Universidad de La Laguna

MEMORIA DEL TRABAJO DE FIN DE GRADO

GRADO EN FÍSICA

SPECTRAL CONVERTING NANOPARTICLES: PRODUCTION, STRUCTURAL AND SPECTROSCOPIC STUDY

Jorge Lorenzo Álvarez

Academic course 2021-2022

4 – 07 - 2022

Supervised by:

Ángel Carlos Yanes Hernández

Francisco Javier del Castillo Vargas

"Quidquid latine dictum sit, altum videtur"

- Anónimo

Index

Universidad
de La Laguna

1. Resumen

El uso de nanopartículas se remonta a la antigüedad en la búsqueda del embellecimiento de piezas artísticas o de alfarería, en las que los artesanos utilizaban, de forma consciente o no, finos polvos de oro u otros metales que hoy en día se clasificarían como nanopartículas. No fue hasta el siglo XX cuando se acuñó el nombre de "materiales nanoestructurados" y desde entonces se han desarrollado innumerables métodos de obtención y caracterización, quedando atrás las rudimentarias técnicas del pasado. En los últimos años, se ha tomado mayor conciencia del gran potencial que presenta las pequeñas escalas de la materia, desde su uso en electrónica e iluminación con la creación de bombillas LEDs, hasta su uso en medicina para el tratamiento localizado de enfermedades. Actualmente, el foco se encuentra sobre materiales dopados con iones de tierras raras, debido a sus especiales propiedades luminiscentes. En particular, destaca el fenómeno de *up-conversion* con potenciales aplicaciones fotocatalíticas, como la producción de hidrógeno (water-splitting) o la eliminación de contaminantes en aguas; así como aplicaciones médicas como la terapia fotodinámica.

En este Trabajo de Fin de Grado (TFG) titulado "*Spectral converting nanoparticles: production, structural and spectroscopic study*" se presenta la obtención y caracterización estructural y espectroscópica de nanopartículas (NPs) de Sr_2YbF_7, que han sido dopadas con diferentes iones: Eu^{3+} (5 %), Er^{3+} (1 %), Tm^{3+} (0.75 %) y Gd^{3+} (50 %). Además, se ha evaluado su posible uso en procesos de fotocatálisis y en terapia fotodinámica.

Las nanopartículas se han sintetizado por el método solvotermal, el cual requiere de altas presiones y temperaturas moderadas ($\leq$200 ^oC), así como de disolventes orgánicos y surfactantes, consiguiendo una composición, morfología y tamaños deseados. Con este método también se han obtenido de forma satisfactoria estructuras Core@Shell (Sr_2YbF_7: RE^{3+}@Sr_2YF_7) de diferentes tamaños, aumentando de forma considerable la emisión de las NPs.

Tras la obtención de estas NPs, se caracterizaron estructuralmente mediante diferentes técnicas: difracción de rayos X (XRD), microscopía electrónica de transmisión (TEM-HRTEM) y espectroscopía dispersiva de rayos X (EDS). Los patrones de XRD se identificaron con la fase tetragonal de la matriz Sr_2YF_7, con tamaños entre 10 y 15 nm (calculados con la ecuación de Scherrer). Además, las imágenes de TEM-HRTEM confirmaron los resultados obtenidos por XRD y mostraron una distribución uniforme de tamaños. Por último, un análisis de EDS da cuenta de la presencia de Sr, Yb y F como principales constituyentes de las NPs, así como la correcta proporción estequiométrica (2:1:7) esperada de la matriz Sr_2YbF_7.

El análisis espectroscópico de los materiales obtenidos permitió completar la caracterización estructural, además de estudiar los diferentes mecanismos de transferencia de energía que tienen lugar en ellos. En particular, se estudió la emisión de los materiales bajo su excitación con radiación infrarroja, adquiriendo un mayor conocimiento de los procesos up-conversion.

Universidad
de La Laguna

Los espectros de emisión y excitación de las muestras dopadas con $2Eu^{3+}$-$0.75Tm^{3+}$ revelaron la presencia de los iones dopantes en sitios centrosimétricos (se estudió la relación entre las intensidades de las transición $^5D_0 \rightarrow {}^7F_2$ y $^5D_0 \rightarrow {}^7F_1$, conocida como *ratio de asimetría*, R, obteniendo un valor de R=0.25). Mediante espectroscopía de absorción en el infrarrojo, se reveló la presencia de moléculas de ácido oleico en la superficie de las NPs. Además, se destacó la importancia del recubrimiento de las NPs con capas inertes de Sr_2YF_7 en la eficiencia de la luminiscencia.

Para las NPs dopadas con $0.75Tm^{3+}$ y $50Gd^{3+}$-$0.75Tm^{3+}$, se observan procesos *up-conversion* (UC) muy eficientes, con intensas emisiones ultravioletas (UV). A partir del recubrimiento con capas inertes de Sr_2YF_7, se observó un aumento de la emisión global de hasta 36 y 33 veces (respecto a las muestras sin recubrir) de las NPs dopadas con $0.75Tm^{3+}$ y $50Gd^{3+}$-$0.75Tm^{3+}$ respectivamente.

Además, a partir del estudio de la intensidad de emisión en relación con la potencia de la radiación incidente, se reveló la presencia de un mecanismo de competencia entre el decaimiento lineal de los iones emisores y los procesos de up-conversion para despoblar los estados excitados intermedios. En este estudio también se observaron algunos efectos relacionados con la concentración de iones Yb^{3+} en los materiales estudiados.

Para las NPs dopadas con $1Er^{3+}$, también se observaron procesos UC muy eficientes con intensas emisiones en el visible (VIS), en particular la emisión roja en 660 nm, así como un gran incremento de la emisión global al ser recubierto por capas inertes, de hasta 143 veces respecto a las muestras sin recubrir. Además, se ha adquirido un mayor entendimiento de los diferentes mecanismos de transferencia de energía presentes en estos materiales.

Por otro lado, se estudió el potencial uso de las intensas emisiones UV que presentan las muestras dopadas con $0.75Tm^{3+}$ y $50Gd^{3+}$-$0.75Tm^{3+}$ en procesos fotocatalíticos. Para ello se estudió la fotodegradación de azul de metileno (MB), obteniendo valores del 38 % y del 19 % para las NPs dopadas con $0.75Tm^{3+}$ y $50Gd^{3+}$-$0.75Tm^{3+}$ respectivamente. En vista de los resultados, se han propuestos diferentes estrategias de cara a mejorar los procesos de fotocatálisis.

Por último, la intensa emisión roja de las NPs dopadas con $1Er^{3+}$ sugieren su potencial uso en terapia fotodinámica. Para ello, se ensamblaron a estas NPs moléculas de α-ciclodextrina (α-CD), con el objetivo de poder dispersarlas en soluciones acuosas; y, posteriormente, moléculas de azul de metileno (MB) como fotosensibilizadoras. Se realizó un estudio espectroscópico del conjunto, obteniendo prometedores resultados que indican una eficiente transferencia de energía desde los iones de Er^{3+} a las moléculas de MB.

2.   Introduction

Las nanopartículas han sido empleadas desde la antigüedad con motivos estéticos en alfarería o en vidriería, y, actualmente, es un campo de investigación en auge, con numerosas aplicaciones desde la medicina hasta la electrónica. Las nanopartículas sintetizadas han sido obtenidas mediante el método solvotermal, que presenta varias ventajas frente a otras técnicas de síntesis. Se ha descrito de forma breve el fenómeno de "up-conversion", así como el material de estudio del presente trabajo.

Nanoparticle is defined as one whose three spatial dimensions are less than 100 nm and bigger than 1 nm. The prefix "*Nano*" comes from Greek and means dwarf, therefore the nanometer refers to a very small length, being one billionth of a metre. The nanoscale (1-100 nm) is often seen as a turning point in the behaviour and properties of a material, as it is a region halfway between macroscopic sizes and molecular/atomic ones (around angstrom, 1 Å = 0.1 nm). This is the scale where all kind of processes occur, such as the formation of proteins in ribosomes or photoluminiscence processes in materials, and this is the reason why it has been the subject of extensive study in recent years.

However, the use of nanomaterials dates back to antiquity. Many of humankind's inventions, such as the creation of ink by the Egyptians or the use of metal nanoparticles to obtain shiny effect in pottery in Mesopotamia, have been based on nanometric manipulation of matter, weather consciously or not. The use of colloidal gold, which was widespread in ancient times in the field of medicine, is grounded on the utilization of very fine, nanometre-sized particles of this metal. A clear example of the huge potential of nanoparticles is the *Lycurgus cup*. This was designed in the 4th century AD by the Romans using colloidal gold. The cup exhibits very interesting luminescent properties, looking red if illuminated from the inside of it and green if the light is reflected from the outside. [1]

(a) Illuminated from the inside   (b) Illuminated from the outside

Figure 2.1: The Lycurgus cup from the 4th century AD, which looks red if illuminated from the inside and green if illuminated from the outside, due to the use of gold nanoparticles. It is exhibited in The British Museum and it is covered with various scenes representing the death of King Lycurgus. [2]

Universidad
de La Laguna

Nowadays, much is known about the atomic and molecular structure of matter, as well as the macroscopic scale, but relatively little is known about the nanoscale. Because of that, the study of nanostructured materials has evolved rapidly over the last century, with new synthesis and characterisation methods being developed and honed. Techniques such as *X-ray diffraction* or *electron microscopy* have been crucial in the development and study of new nanomaterials with customized properties. [3]

In particular, the creation and use of nanoparticles (NPs) might be highlighted due to their versatility in a variety of applications. NPs are ideal for use in medicine, photonics or communications due to their size and easy integration into different systems, weather living or non-living. [4]

Currently, *up-conversion* nanoparticles (UCNPs) are under the spotlight of study for the use in a multitude of different fields of science and technology, as they are able to transform the incident radiation into a more energetic one. These UCNPs can be used in photocatalysis processes, in medicine, in the improvement of photovoltaic cells, the production of LEDs, etc.
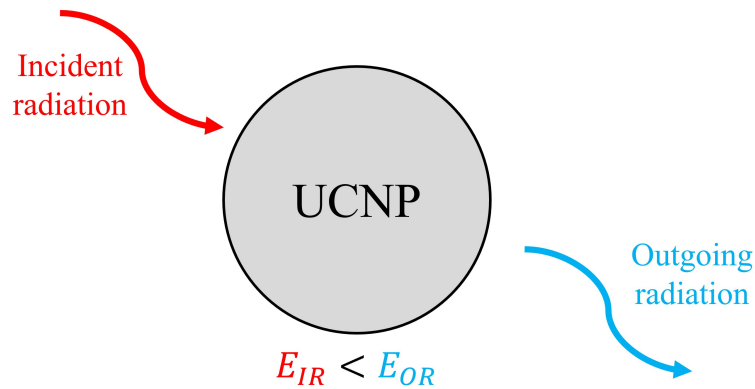

Figure 2.2: Schematic diagram of UCNPs performance. The energy of the incident radiation, E_{IR}, is lower than the energy of the outgoing radiation, E_{OR}.

The *up-conversion* phenomenon (UC) or *Anti-Stokes shift luminiscent* is an optical process in which a long-wavelength excitation is converted into short-wavelength emission with higher energy. This ability is the key for the multiple applications of the UCNPs [5].

In the materials studied, take place *energy transfer up-conversion* (ETUC), in which two, generally different, ions function as sensitiser and emitter (see Figure 2.3). The sensitiser ion first absorbs an infrared photon and moves to an excited state. Energy transfer (ET) promotes the emitter to an intermediate excited state (level 2) while the sensitiser falls to the ground state. The emitter can be excited to a higher level (state 3) by ET from another sensitiser which has absorbed a photon (left case in the figure) or by absorption of a photon by the emitter itself (right case of the figure). Finally, radiative emission from the highest level (3) occurs. It is necessary that the sensitiser and the emitter are spatially close and that the intermediate state of the emitter is lower than the sensitiser excited one. This is of great importance in the choice of dopants.[6]
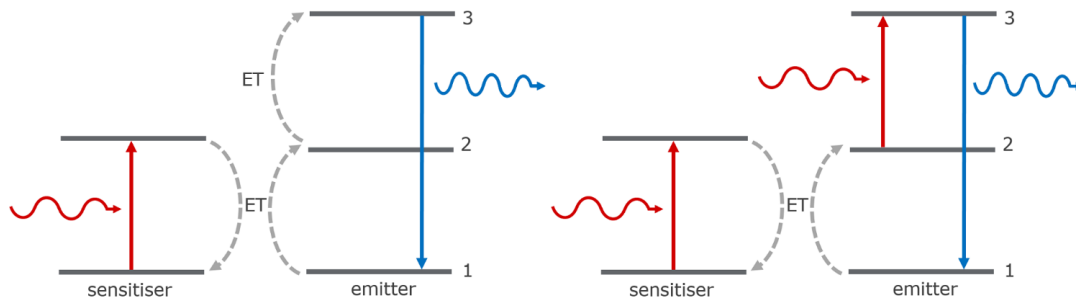
Figure 2.3: Schematic diagram of *energy transfer up-conversion* process. The red curved lines represent an incident photon while the red and blue straight lines represent the excitation or de-excitation of the ions, respectively.

There are numerous methods for obtaining NPs, each with its own advantages and disadvantages. The nanomaterials in this work have been obtained using the solvothermal method, as it has attractive advantages over other synthesis methods. This technique makes it possible to synthesise a large number of NPs with optimal size, morphology and chemical composition in a rationally easy and inexpensive way. It does not involve high temperatures, however, it does not allow continuous monitoring of the sample during production. [7]

As mentioned above, Rare Earth ions (RE^{3+}) are intentionally introduced into a initial crystalline matrix in small quantities, i.e. the crystal is doped with RE^{3+}, in order to control its optical properties. Specifically, the aim is to make the materials obtained undergo *up-conversion* processes.

This Trabajo de Fin de Grado (TFG) presents the production and study of different up-conversion nanoparticles (UCNPs) doped with Rare Earth ions (RE^{3+}) with intense ultraviolet (UV) or visible (VIS) emissions and the main goal of their application in photocatalysis (generation of hydrogen by water-splitting processes or the treatment of water pollutants) and in photodynamic therapy, respectively. For this TFG, a Sr_2YbF_7:RE^{3+} matrix has been selected, due to its great thermal stability and low phonon energy, reducing the non-radiative de-excitation losses and improving the radiative emission of the dopant ions [8]. On the other hand, the large absorption cross-section at 980 nm of Yb^{3+} ions, along with the high concentration of these ions, enhance the energy transfer between ions and the luminescence of the materials obtained in the up-conversion processes [9]. Finally, the chosen dopant ions are Eu^{3+} (as probe structural ion), Tm^{3+} and Gd^{3+} (for their intense UV emissions) and Er^{3+} (for their strong red emission). In addition, it has been taken into account that their ionic radii are similar to that of Yb^{3+} [10], so that their incorporation into the matrix is favoured (dopant ions can substitute Yb^{3+} in the crystal lattice).

3.   Objectives

The main goals pursued in carrying out this TFG are the following:

- **Obtain new nanostructured materials by solvothermal method**

- **Structural characterisation of the resulting nanostructured materials:**

  - X-Ray Diffraction (XRD): determination of crystalline phase and average size of the nanoparticles.

  - Transmission Electron Microscopy (TEM - HRTEM): study of morphology, size distribution and crystalline structure of the materials obtained.

  - Energy Dispersive X-Ray Spectroscopy (EDS): study of the chemical composition of the NPs.

- **Spectroscopy characterisation:**

  - Luminescence Spectroscopy: characterisation of the crystalline environment of the dopant ions

  - Energy transfer mechanisms: study of up-conversion processes occurring in the materials.

- **Photocatalysis experiment:** study of possible applications of nanomaterials for hydrogen generation or wastewater treatment.

- **Photodynamic therapy experiment:** study of possible applications of these nanomaterials for photodynamic therapy.

Universidad
de La Laguna

4. Experimental Methodology

Se detalla de forma breve las propiedades de los iones de tierras raras y su estructura electrónica, así como los tipos de desexcitaciones en la matriz empleada. También se explica en detalle la obtención de las NPs mediante el método solvotermal, además de las características técnicas de los equipos empleados en la caracterización estructural y espectroscópica. Finalmente, se detalla el experimento de fotocatálisis para el estudio de potenciales aplicaciones en el tratamiento de contaminantes en agua y la generación de hidrógeno (water-splitting); así como la preparación y estudio de NPs para su uso médico en terapia fotodinámica.

4.1. Properties of RE³⁺ ions

The RE³⁺ ions or the "*lanthanide series*" starts with Lanthanum (La, Z = 57) and ends with Lutetium (Lu, Z = 71), making a total of 14 elements of the Periodic Table. Lanthanide elements form stable oxides, phosphates, sulfides and halides and their peculiar properties are due to their electronic structure. The RE³⁺ ions have $4f$ shell incomplete and the electronic configuration is $5p^6 6s^2 4f^n$, where each ion has a different number of unpaired electrons in the $4f$ shell. This gives these ions curious magnetic and optical properties when interacting with ultraviolet, visible and infrared radiation. [11]

An important property of this group is that the ionic radius decreases with increasing atomic number, a phenomenon known as "*lanthanide contraction*" (see Figure 4.1). This is due to the weak shielding effect between $4f$ electrons and the increasing mass and atomic number of the nuclei. [12]
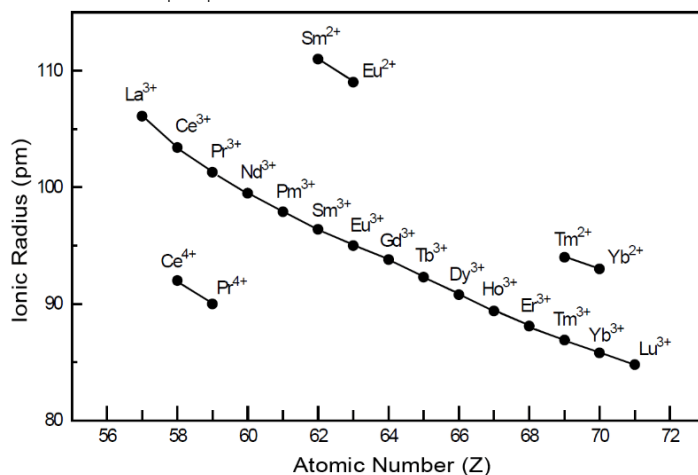

Figure 4.1: Ionic radius vs. atomic number for *lanthanide series.* [13, Fig. 2.4]

In the light of these promising properties derived from the electronic structure of these RE³⁺ ions, a brief characterisation of the energy levels should be made. It is well-known that the energy levels of hydrogen-like atoms are describe in terms of the quantum numbers n (related to the radial component of the description), l (related to the orbital angular momentum), m_l (related to the z-axis projection of the orbital angular momentum), s (related with the electron spin) and m_s (related with the z-axis projection of the electron spin).

Universidad
de La Laguna

Nevertheless, for multielectron atoms these are not the right quantum numbers. Instead of these, it is necessary to introduce the total orbital angular momentum L and the total spin momentum S of the atom, along with their corresponding projections: M_L and M_S respectively. In addition, for heavy atoms exist a spin-orbit coupling energy. It is usual to use the Russsell-Saunders formalism to describe the energy levels of RE^{3+} ions, in which the *L-S coupling* is described with a new quamtum number J and its z-axis projection M_J. [14]

Using this formalism, the energy levels are uniquely characterised in terms of five quantum numbers $|n, L, S, J, M_J\rangle$, each state being $2J + 1$ times degenerate (there are $2J + 1$ states with the same energy). Now the states are denoted by a new spectroscopic notation: $^{2S+1}L_J$ where $L = 0$ corresponds to state S, $L = 1$ to state P and continues in the usual manner. This is a simple way of knowing the energy levels, as well as the transition selection rules. For example, only transitions with $\Delta J = 0, \pm 1$ (except $J = 0 \rightarrow J = 0$) are possible. [14]

It might be said that, although the Russell-Saunders formalism is applicable to light atoms ($Z < 30$) and the JJ coupling model must be used for the *lanthanide series*, sometimes for excited configurations such as those of the ions used, L-S coupling occurs and the energy levels are described as shown above. In Figure 4.2 the RE^{3+} ions energy levels are shown.
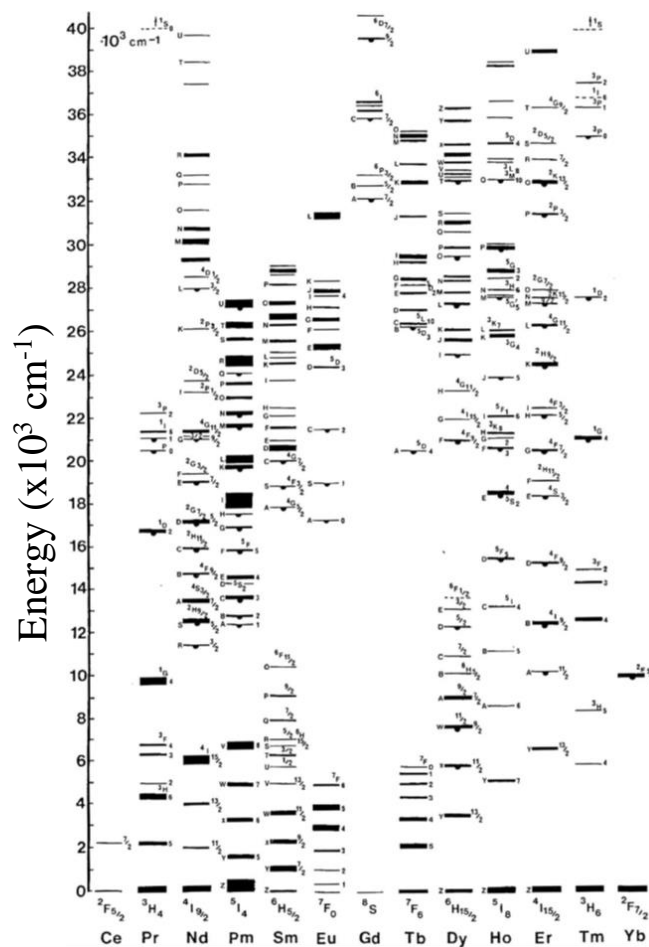

Figure 4.2: RE^{3+} ions energy levels (Dieke diagram). [15, Fig. 3]

When these ions are introduced into a crystalline matrix, their emission mechanisms are affected and strongly depend on the host-dopant interaction. This is due to the small Stark splitting that the degenerate energy levels undergo as a result of the crystal field created by the ions forming the crystalline lattice. However, this splitting is much smaller than the difference between different energy levels. [16]

The small perturbation (less than 100 cm^{-1}) allows to obtain narrow line spectra of lanthanide-doped NPs, due to electron transitions in the 4f layer. The interaction of the $4f$ electrons with the crystal field of a host material is small and the level of the RE$^{\mathbf{3+}}$ ions are greatly unchanged. Due this and to their particular luminescence, they are used in many materials as dopants. [17]

Once this electronic structure is known, the NPs can be designed in such a way that the dopant ions are promoted to excited states and their de-excitation can be studied. There are two main types of de-excitation:

- <u>Radiative de-excitation</u>: produces the emission of photons. As it has been said this type of de-excitation depends on the host-dopant interaction.

- <u>Non radiative de-excitation</u>: produce the energy transfer with the crystal lattice (phonons) or with the neighbouring ions.

The possible applications of the NPs obtained focus on their radiative emissions. For this reason, crystalline matrices that minimise non-radiative phonon de-excitations, which represent an undesired loss of energy, must be sought. The Sr_2YbF_7 matrix meets these requirements, in addition to other interesting properties such as a small size.

4.2. Obtaining nanostructured materials

The NPs have been obtained by the solvothermal method, which does not involve the use of high temperatures, vacuum environments or inert gases that make the synthesis of the materials more expensive and technically difficult, as is the case with co-precipitation or thermal decomposition methods. Solvothermal synthesis requires high pressures and moderate temperatures ($\leq 200\ ^oC$), usually above the critical point of the solvents used. Organic solvents, such as alcohols or amines, and surfactants (which influence the contact surface between two phases by reducing the surface tension), such as oleic acid (OA), are used in this process. The main advantage of this method is the technical simplicity and the high quality of the NPs obtained, without producing toxic products and relatively cheaply. This has placed solvothermal synthesis at the forefront of nanomaterial production. [18]

A total of 11 samples were prepared with different dopants and purposes:

NANOPARTICLE		PURPOSE
Sr$_2$YbF$_7$:(2Eu-0.75Tm)	$\rightarrow$	Sr$_2$YbF$_7$ NPs doped with 0.75% Tm^{3+} and 2% Eu^{3+} for structural characterisation and to study the chemical environment around the dopant ions.
Sr$_2$YbF$_7$:0.75Tm	$\rightarrow$	Sr$_2$YbF$_7$ NPs doped with 0.75% Tm^{3+} for up-conversion processes and photocatalytic applications study. Up to two inert shells were added to this sample.
Sr$_2$YbF$_7$:(50Gd-0.75Tm)	$\rightarrow$	Sr$_2$YbF$_7$ NPs doped with 0.75% Tm^{3+} and 50% Gd^{3+} for up-conversion processes and photoctalytic applications study. Up to two inert shells were added to this sample.
Sr$_2$YbF$_7$:1Er	$\rightarrow$	Sr$_2$YbF$_7$ NPs doped with 1% Er^{3+} for structural and spectroscipic characterisation, as well as for medical applications study. Up to two inert shells were added to this sample.

Table 4.1: NPs obtained with the solvothermal method.

To obtain the necessary high pressures and for temperature control, a Teflon autoclave and a conventional mufla oven are used, respectively (see Figures 4.3a and 4.3b).

First, 10 ml of ethanol and 20 ml of oleic acid were mixed, to which a solution of 2 ml of water and 0.6 g of NaOH was added and shaken vigorously for 30 minutes until a homogeneous, clear solution was obtained.

Then, 0.5 mmol of Cl_3Yb (99.998% *Sigma-Aldrich*) and $Eu(CH_3COO)_3$ (99.9% *Sigma-Aldrich*), $Er(CH_3COO)_3$ (99.9% *Sigma-Aldrich*), $Tm(CH_3COO)_3$ (99.9% *Sigma-Aldrich*), $Gd(CH_3COO)_3$ (99.9% *Sigma-Aldrich*) were added according to the sample to be made, following the appropriate ratios, and dissolved in 2 ml of water. Subsequently, 1 mmol of $Sr(CH_3COO)_3$ (99.995% *Sigma-Aldrich*) dissolved in 2 ml of water was added.

Finally, 2 ml of aqueous solution containing 3.5 mmol of NH_4F ($\geq 98\%$ *Sigma-Aldrich*) was added, and after 30 minutes of vigorous stirring, the whole mixture was poured into a 50 ml stainless steel-lined Teflon autoclave. The autoclave, tightly closed, was heat treated at 200 ^oC for a full day (24 hours).

After this time, the autoclave cooled down naturally to room temperature and centrifuging was performed at 4000 rpm for 15 minutes to separate the NPs formed from the different solvents. Then, the resulting product was dispersed in 2 ml of cyclohexane and precipitated with 6 ml of ethanol, both for 15 minutes. This process of washing the samples was carried out twice in succession, ending with a final centrifuging and drying at 60 ^oC for approximately 12 hours.

The same procedure was followed for the preparation of the Core@Shell (C@S) and Core@Shell@Shell (C@S@S), adding 75 mg of core (sample to be coated) dispersed in 4 ml of cyclohexane after the last 30 minutes of joint agitation, followed by another 30 minutes of vigorous agitation before placing it in the autoclave. The washes were carried out in exactly the same way. Figure 4.3 shows the centrifuge and magnetic stirrers used.

(a) Autoclave
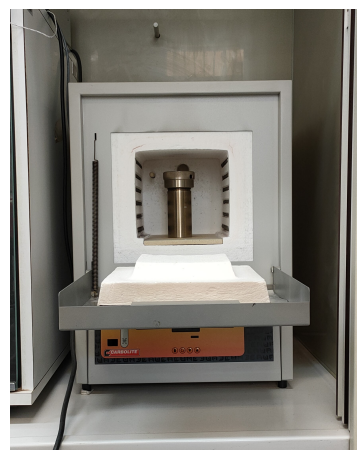
(b) Conventional mufla oven

(c) Magnetic stirrer

(d) Centrifuge

Figure 4.3: Some material used in the production of the NPs.

The synthesis was done in the Nanomaterials Laboratory of Physics Section (Science Faculty of Universidad de La Laguna).

4.3. Experimental techniques and equipment for characterisation

Technical aspects of the instrumentation and the procedures used in the structural and spectroscopic characterisation, as well as in the study of photocatalysis applications, are detailed below.

4.3.1. Structural characterisation

Three different techniques were used for the structural characterisation of the NPs: X-Ray Diffraction (XRD), Transmission Electron Microscopy (TEM) and Energy Dispersive X-Ray Spectroscopy (EDS). Each provides information about the size, morphology and chemical composition of the NPs. The measures were provide by the SEGAI (*Servicios Generales de Apoyo a la Investigación*), a service of the Universidad de La Laguna with multiple laboratories and instrumentation for collective use.

XRD measurements were carried out with a *Panalytical X´Pert PRO* diffractometer, which consists of a $K_{\alpha,1,2}$ radiation source, a primary monochromator and an *X'Celerator* detector. It allows a 2θ angular range between -40° and 160° [19]. For the use of this facility, the NPs were grounded with an agate mortar to a fine powder which was placed and lightly pressed into a holder that is inserted into the measuring device. The XRD patterns were collected in the 2θ range from 20° to 80°.

Transmission Electron Microscopy (TEM - HRTEM) images were obtained with the *JEOL JEM 2100* electron microscopy, which operates with an acceleration voltage of 200 kV and achieves a resolution of 0.23 nm [20]. The NPs were dispersed in ethanol and subsequently placed in a copper and carbon grid. This device was also used to get the EDS patterns.

(a) *Panalytical X´Pert PRO* diffractometer   (b) *JEOL JEM 2100* electron microscopy

Figure 4.4: XRD and TEM devices used for the structural characterisation.

4.3.2. Spectroscopic characterisation

For the spectroscopic characterisation a spectrofluorometer manufactured by *PTI: Photon Technology International* was used (see Figure 4.5). This device consists of the following elements:

- Radiation source: an infrared (980 nm) variable power laser (*Power Technology, Inc*) was used as the excitation source to obtain the emission pattern of the NPs. For excitation spectra, a Xenon Lamp (*PTI: Photon Technology International* - 150 W) was used. Concerning to the focalization of the laser beam over the sample, a 50 mm lens was used.

- Wavelength selector: a set of monochromators installed in the device allow selection of wavelength.

- High-pass filters: avoid the detection of harmonics and stray light.

- Detection system: consists of a R-928 photomultiplier, which converts incident photons into an electrical signal.

- Control system: software FeliX32 allows the control of the monochromators, the acquisition and processing of the spectra. In addition, corrects the spectra taking into account the response of the detector.
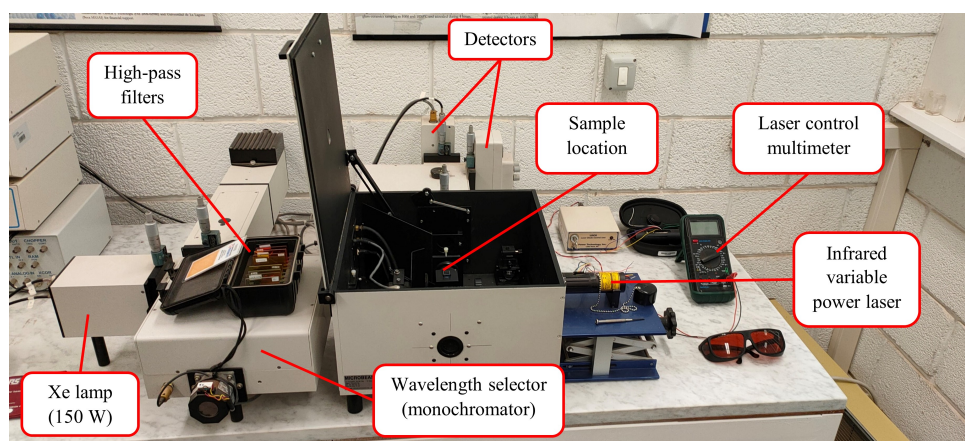

Figure 4.5: Fluorometer and its components.

The spectroscopic study was carried out at room temperature in all cases. For the corresponding measurements, the NPs were dispersed in 1 ml of cyclohexane in such a way that they represent 1% of weight. A drop of oleic acid can be added to help the disperssion of the NPs. This is done in a quartz cuvette, since this material has a high UV-VIS transmittance (range of interest for applications).

The measures were done in the Nanomaterials Laboratory of Physics Section (Science Faculty of Universidad de La Laguna).

4.4.   Photocatalytic applications: methodology

As potential application of NPs with high ultraviolet (UV) emission is the degradation of water pollutants by photocatalysis, which is widely studied around the world. For the photocatalysis experiment, an aqueous solution of methylene blue (MB) with a 10 ppm concentration (1 mg of MB in 100 ml of H_2O) was prepared. Assisted by a *DS5 Dual Beam UV-Vis* spectrophotometer manufactured by *Edinburgh Instruments* (see Figure 4.6), the required absorption spectra were obtained by comparison between a reference and the studied sample. First of all, the baseline for the quartz cuvettes was obtained and then, the MB aqueous solution was measured to check that its optical density (OD) was around 2.0 for a wavelength of 664 nm.
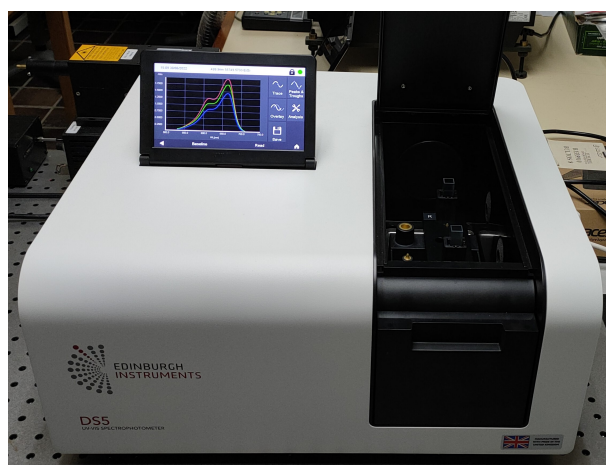

Figure 4.6: *DS5 Dual Beam UV-Vis.* spectrophotometer used.

Afterward, a solution of 6 ml of MB and 4.5 g of TiO_2 was prepared and stirred for a few minutes in dark conditions. Later, 2.5 ml of this solution was extracted and placed in a quartz cuvette to perform the photocatalysis of MB. On the top of the cuvette, a tiny quartz capillar was located with NPs dispersed in cyclohexane (1% of weight). The whole emsemble was fitted into the fluorometer (see Figure 4.5), where the infrared laser, with a wavelength of 980 nm and power of 300 mW, was focused on the NPs by using a 50 mm lens, so that their intense UV emissions would activate the TiO_2 and photocatalysis would take place. The MB-TiO_2-NPs set was exposed to the infrared radiation during 1 hour and 30 minutes, while the rest of the MB-TiO_2 solution was stirred in dark conditions. Emission spectra were obtained every 20 minutes from the irradiated cuvette using the fluorometer in order to verify the experiment.

After the irradiation time, both solutions (MB-TiO_2-NPs and MB-TiO_2) were centrifuged during 15 minutes at 3500 r.p.m. in order to separate the NPs and the TiO_2 from the aqueous MB solution. Finally, the absorption spectra of the MB-TiO_2 solution stirred in dark conditions and MB-TiO_2-NPs set exposed to the infrared radiation were obtained. The first one provides information about the adsorption of the TiO_2 in the solution and the second one, about the effectiveness of the photodegradation.

Only NPs with two inert shells (C@S@S) were studied as they presents the more intense UV emissions. This experiment was carried out in the Optical Spectroscopy Laboratory and the Nanomaterials Laboratory of Physics Section (Science Faculty of Universidad de La Laguna).

Universidad
de La Laguna

4.5.   Medical applications: obtainment of NPs for photodynamic therapy

As it is explain later, for the study of photodynamic therapy as a potential application, it is necessary firstly to incorporate α-cyclodextrin molecules (α-CD) to the NPs and then to load them with photosensitizers (in this case Methylene Blue, MB). Here the incorporation of α-CD to Sr_2YbF_7:1Er and the MB loading is presented.

Firstly, in order to transfer Sr_2YbF_7:1Er into an aqueous phase, the α-CD must be added as surface modifier. For that, 5 mg of Sr_2YbF_7:1Er NPs was added to an aqueous solution containing α-CD (20 mg/ml) and ultrasonically treated for 15 minutes at room temperature. Next, this solution was centrifuged (15 minutes at 4000 r.p.m.) in order to separate the α-CD-NPs from the aqueous phase. Then the products were washed three times with deionized water and dried at 60 ^oC for a whole day.

For the chosen photosensitizer loading, 5 mg of α-CD-NPs was dispersed in 1 ml of dimethyl sulfoxide (DMSO) and MB (250 μM). The whole solution was stirred for 20 hours in dark conditions at room temperature. The resulting complexes MB-α-CD-Sr_2YbF_7:1Er were collected by centrifugation, washed with buffer phosphate three times and dried at 60 ^oC for a whole day.

To check the successful growth of the MB-α-CD-Sr_2YbF_7:1Er complexes, 1 mg was dispersed in 1 ml of acetonitrile. The final solution was study with the spectrofluorometer (see Figure 4.5) and compared with the Sr_2YbF_7:1Er NPs.

The synthesis and measures were done in the Nanomaterials Laboratory of Physics Section (Science Faculty of Universidad de La Laguna).

5. Results and Discussion

Los resultados obtenidos se dividen en cuatro secciones. En la primera se presenta el estudio espectroscópico a partir de las medidas de XRD, TEM - HRTEM y EDS, detallando el tamaño, distribución y composición química de las NPs obtenidas. Se expone únicamente la caracterización estructural de unas pocas NPs, siendo todo ello aplicable para el resto de materiales sintetizados. La segunda sección se dedica al estudio espectroscópico a partir de los espectros de emisión y excitación. Las emisiones sensibles al entorno del Eu³⁺ se utilizan como complemento de la caracterización estructural y se estudia en detalle los procesos de up-conversion que tienen lugar en las NPs dopadas con Tm³⁺, Gd³⁺ y Er³⁺. Las últimas dos secciones se dedican al estudio de aplicaciones de los materiales obtenidos. En primer lugar, se detalla el experimento de fotocatálisis con las NPs dopadas con Tm³⁺ y Gd³⁺, que presentan intensas emisiones ultravioletas. Los resultados obtenidos suguieren el uso potencial en la creación de H₂ por water-splitting o el tratamiento de aguas residuales. Por último, se realiza una primera aproximación a aplicaciones médicas como la terapia fotodinámica, utilizando las emisiones rojas de las NPs dopadas con Er³⁺.

The results obtained can be divided into three different sections, as follows:

- Firstly, the structural characterisation by XRD, TEM - HRTEM and EDS measurements is presented. The production of Sr_2YbF_7 NPs by the solvothermal method is confirmed and their size, distribution and chemical composition are studied. Only the structural characterisation of a few NPs is presented, being applicable for the rest of the synthesised materials. In particular, the XRD patterns of the samples doped with $2Eu^{3+}$-$0.75Tm^{3+}$, $50Gd^{3+}$-$0.75Tm^{3+}$ and $1Er^{3+}$ are set out. Only TEM images and EDS analysis of Sr_2YbF_7:1Er NPs are presented.

- The second section is devoted to the spectroscopic study of the samples doped with $2Eu^{3+}$-$0.75Tm^{3+}$ based on their emission and excitation spectra. The spectroscopic study of $0.75Tm^{3+}$, $50Gd^{3+}$-$0.75Tm^{3+}$ and $1Er^{3+}$ doped NPs is also set out. In addition, the different energy transfer mechanisms that take place in these NPs are analysed.

- Then, the results of the photocatalysis experiments are presented, concluding a potential application of these NPs in H_2 generation and the treatment of pollutants in wastewater. This experiment was carried out with the Core@Shell@Shell NPs doped with $0.75Tm^{3+}$ and $50Gd^{3+}$-$0.75Tm^{3+}$.

- In the last section, a brief approach to the use of $1Er^{3+}$ doped UCNPs in photodynamic therapy is presented.

5.1. Structural characterisation

The structural characterisation shown in the following subsections was carried out from the XRD patterns of the $2Eu^{3+}$-$0.75Tm^{3+}$, $50Gd^{3+}-0.75Tm^{3+}$ and $1Er^{3+}$ doped NPs, as the other samples showed the same morphology and size distribution. TEM images and an analysis of the chemical composition from EDS measurements of Sr_2YbF_7:1Er are also presented.

5.1.1. X-Ray Diffraction (XRD)

The XRD patterns of the indicated NPs are shown in Figure 5.1. The measurements considerably coincide with the standard peaks of the Sr_2YF_7 tetragonal phase (JCPDS 53-0675) without any additional phase, thus confirming the formation of the NPs with this phase. The differences are due to the use of Yb^{3+} ions instead of Y^{3+}, as will be discussed below.
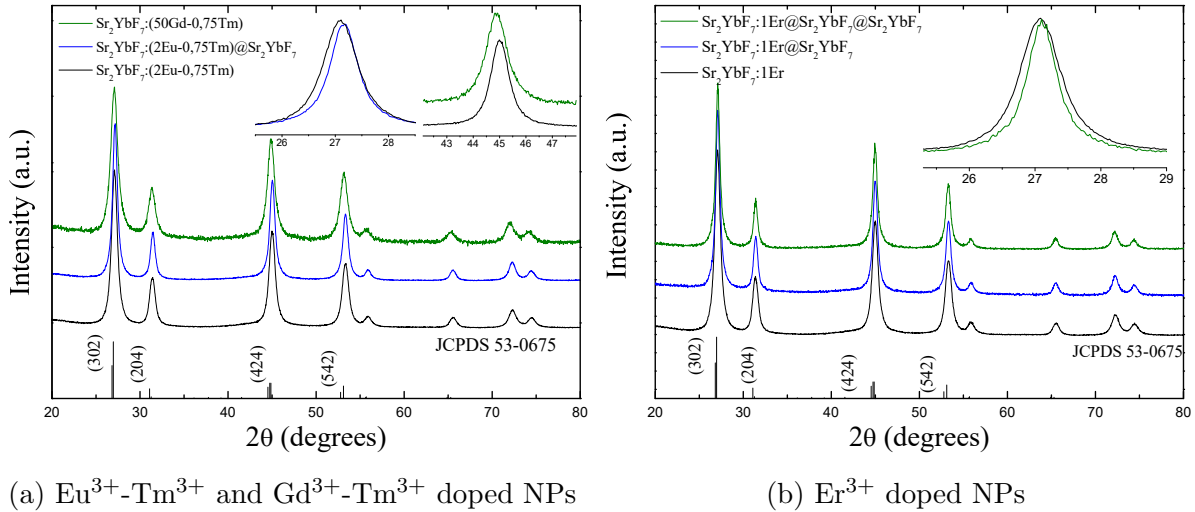
(a) Eu^{3+}-Tm^{3+} and Gd^{3+}-Tm^{3+} doped NPs   (b) Er^{3+} doped NPs

Figure 5.1: XRD patterns of the indicated NPs, as well as the theoretical peaks of the tetragonal phase of Sr_2YbF_7. Magnifications shown are for comparative purposes. The diffraction planes at each standard peak are also shown.

It is observed that the XRD patterns in all cases are slightly deviated to the right from the theoretical peaks. This is due to the difference in ionic radii between the Yb^{3+} ($r_{Yb^{3+}} = 0.985$ Å) and Y^{3+} ($r_{Y^{3+}} = 1.019$ Å) ions. This also produces the leftward shift of the $50\%Gd^{3+}$-$0.75\%Tm^{3+}$ doped NPs' peaks (as ionic radii of Gd^{3+} ions is larger, $r_{Gd^{3+}} = 1.053$ Å, than the Yb^{3+} one), confirming that Gd^{3+} replaces Yb^{3+} in the matrix, deviating the pattern from the Eu^{3+} doped NPs (see right-side magnification of the XRD patterns in Figure 5.1a).

Furthermore, the successful growth of the inert shells can be conclude, as a slight deviation of the peaks between the different Eu^{3+} and Er^{3+} doped samples can be observed (see amplification of the XRD patterns in Figure 5.1). On the other hand, the narrowing of the XRD peaks also imply the Sr_2YF_7 shell growth. This can be seen in the magnifications in the range of 26 - 28 degrees of Figures 5.1a and 5.1b.

The average size of the NPs can be obtained from the peak of maximum intensity by using the Scherrer equation:

$$D = \frac{K \cdot \lambda}{\beta \cdot cos(\theta)} \tag{5.1}$$

Where D is the average size of the NPs, K is a dimensionless shape factor dependent on the instrument and the sample (in this case $K = 0.9$), λ is the X-Rays wavelength (in this case $\lambda = 0.1540610 \ nm$), β is the line broadening at half the maximum intensity in radians and θ is the Bragg angle. [21]

It is understandable from Equation 5.1 why the narrowing of the peaks indicates the growth of the inert shells on the NPs surfaces (the average size is inversely proportional to the line broadening). Table 5.1 shows the results obtained with this equation. The growth of the inert layer on the corresponding samples is also checked, as well as the proportion of core in each sample, i.e. the proportion of active ions for spectroscopic study.

Nanoparticle	Average size (nm)	Shell thickness (nm)	Core proportion (%)	Active factor
Sr_2YbF_7:(0.75Tm-2Eu)	10.6	-	100	1
Sr_2YbF_7:(0.75Tm-2Eu)@Sr_2YF_7	12.9	1.15	55.48	1.80
Sr_2YbF_7:0.75Tm	10.18	-	100	1
Sr_2YbF_7:0.75Tm@Sr_2YF_7	13.5	1.66	42.88	2.33
Sr_2YbF_7:0.75Tm@Sr_2YF_7@Sr_2YF_7	15.82	1.16	26.41	3.79
Sr_2YbF_7:(50Gd-0.75Tm)	8.74	-	100	1
Sr_2YbF_7:(50Gd-0.75Tm)@Sr_2YF_7	10.57	0.865	47.75	2.09
Sr_2YbF_7:(50Gd-0.75Tm)@Sr_2YF_7@Sr_2YF_7	12.7	1.065	33.72	2.96
Sr_2YbF_7:1Er	10.3	-	100	1
Sr_2YbF_7:1Er@Sr_2YF_7	13.15	1.425	48.05	2.08
Sr_2YbF_7:1Er@Sr_2YF_7@Sr_2YF_7	15.76	1.305	27.92	3.58

Table 5.1: NPs structure parameters.

The *core proportion* has been obtained by calculating the fraction of volume occupied by the core in each case.

The *active factor* shown in the right column of Table 5.1, is the inverse of the *core proportion* and it is the value by which the intensity of the different spectra of the samples studied in the following sections should be multiplied. The reason behind this is the preparation of the NPs dispersed in ciclohexane at 1% by weight for the spectroscopic study, since, as can be inferred from Table 5.1, the samples covered with inert shells have a lower proportion of core, i.e. spectroscopically active ions. By preparing all samples in the same way, the comparison of the emissions would not be fair as there is not the same amount of luminescent ions between Core, Core@Shell and Core@Shell@Shell NPs doped with the same RE^{3+} ions. This has already been considered in the spectra presented in the spectroscopic study.

5.1.2.   Transmission Electron Microscopy (TEM - HRTEM)

In addition, TEM images of the Core and C@S@S Er^{3+} doped NPs were used to confirm the structural characterisation performed with the XRD patterns. The size of the NPs, their structure and morphology are checked (see Figure 5.2). Figure 5.2a shows TEM images of Sr$_2$YbF$_7$:1Er and Figure 5.2b shows the HRTEM images of this core sample doped with Er^{3+} ions. The lattice fringes are very easy to identify, which indicates a very crystalline environment in the NPs.
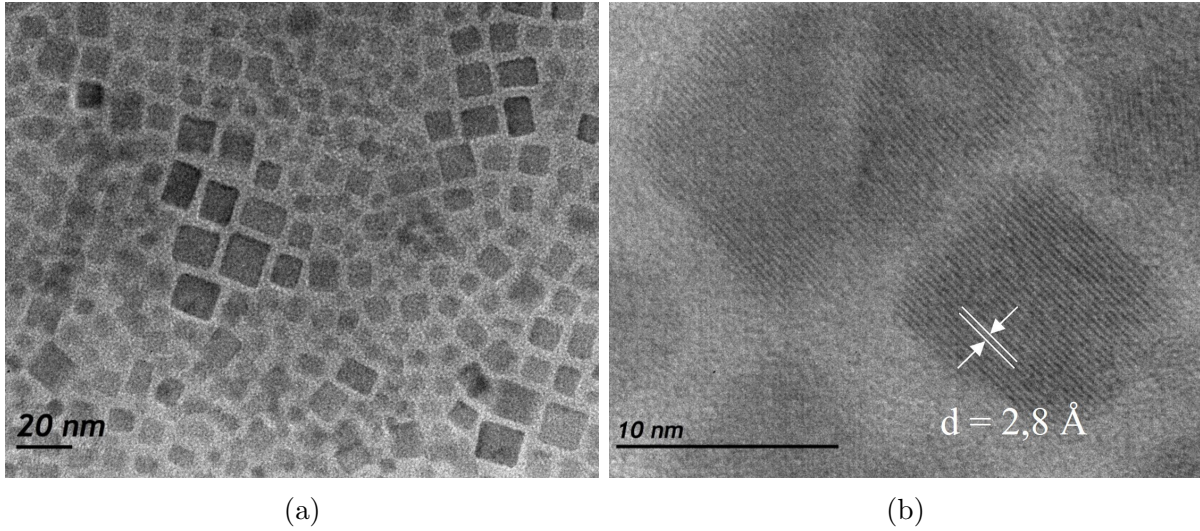

(a)   (b)

Figure 5.2: TEM images of Sr$_2$YbF$_7$:1Er (a) and HRTEM images (b), where the lattice fringe spacing is indicated, d.

Uniform and dispersed NPs are clearly observed over the gray background and that the size of them is around 10 nm, as concluded from the XRD patterns. Similar TEM-HRTEM images were gattered for C@S@S samples (not shown), with clearly dispersed NPs and average sizes around 15 nm.

For the Core NPs, the lattice fringe spacing has a value of 2.8 Å, which correspond to the (204) plane of the Sr$_2$YF$_7$ tetragonal phase. This can be conclude by using the Bragg equation (Eq. 5.2). [22]

$$n\lambda = 2dsen(\theta) \tag{5.2}$$

Where n is a integrer number, λ is the incident wavelength radiation, d is the spacing of the lattice planes and θ is the incident radiation angle. It has been obtained that $\theta \approx 15.9^o$, which corresponds to the (204) plane (see Figure 5.1).

5.1.3. Energy Dispersive X-Ray Spectroscopy (EDS)

Finally, EDS analyses (see Figure 5.3) confirmed the presence of Sr, Yb, Y and F as the main constituents in the samples obtained. There is no appreciable Er^{3+} signal due to the low concentration of this ion in the NPs. The C and Cu signals come from the grating used in the measurements.

For the Core NPs, the atomic percentages content of Sr (21.81%), Yb (11.38%) and F (66.81%) confirm the stochiometric ratio of Sr_2YbF_7:1Er (2:1:7). On the other hand for the C@S@S NPs, the ratio between the atomic percentages content of Yb (2.93%) and Y (9.19%) confirms that there is 31.88% of Yb vs. the amount of Y, supporting the calculation made in Table 5.1 (*core proportion* column).
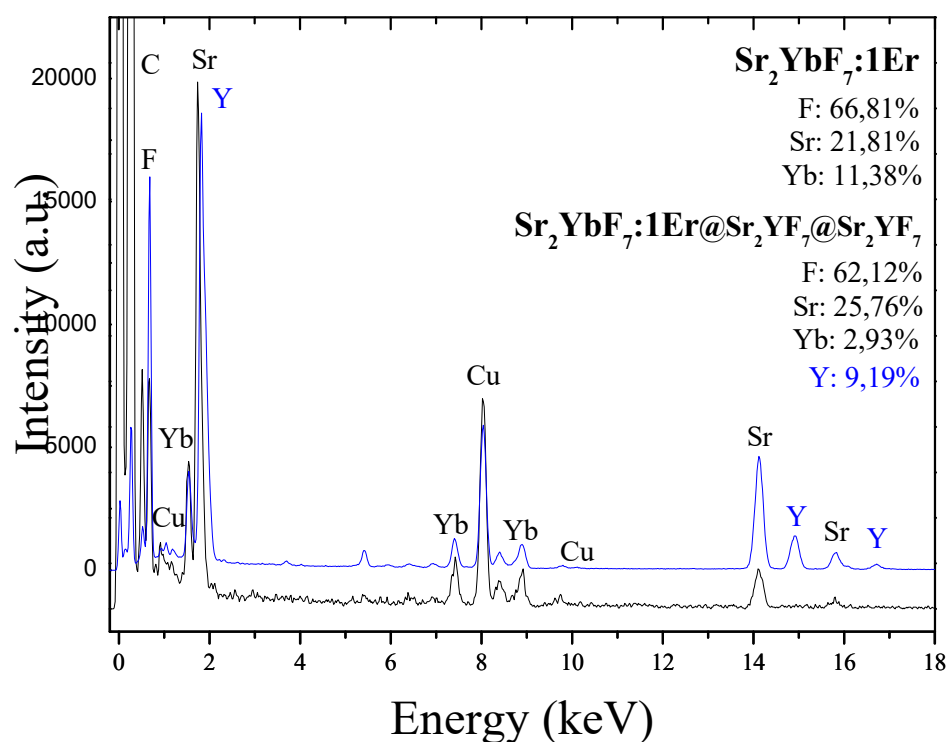

Figure 5.3: EDS pattern of Sr_2YbF_7:1Er. The atomic percentage content of each chemical species is written down in the figure.

5.2. Spectroscopic study

In order to complete the structural analysis, the emission and excitation spectra of the $2Eu^{3+}$-$0.75Tm^{3+}$ samples were analysed, as they provide information of the environment in which the dopant ions are found.

Next, the study of the up-conversion processes in samples doped with $0.75Tm^{3+}$ and $50Gd^{3+}$-$0.75Tm^{3+}$, allows to evaluate the potential of these NPs in photocatalysis processes.

Then, the study of the up-conversion processes in samples doped with $1Er^{3+}$, allows to evaluate the potential of these NPs in photodynamic therapy.

Finally, the effect of coating with inert shell is observed in all the NPs, considerably increasing the emission of the samples by reducing the energy loss due to quenching processes.

5.2.1. Eu^{3+}-Tm^{3+} doped NPs

The structural characterisation of the nanostructured materials is rounded off by a spectroscopic study of Sr_2YbF_7:(2Eu-0.75Tm) and Sr_2YbF_7:(2Eu-0.75Tm)@Sr_2YF_7 is carried out. Figure 5.4 shows the emission and excitation spectra of the Eu^{3+}-Tm^{3+} doped NPs.
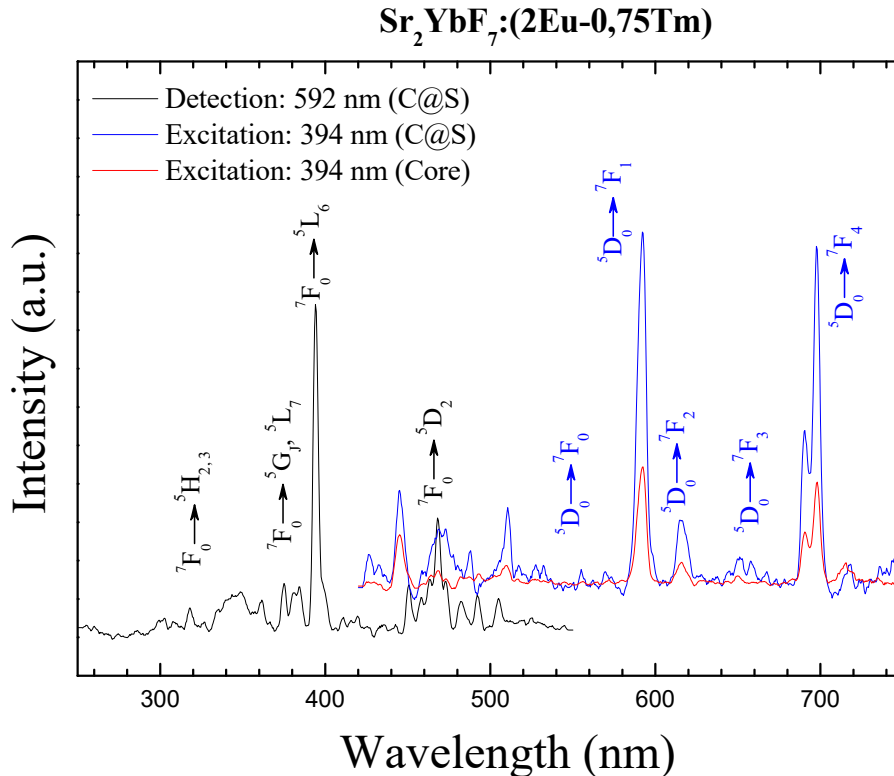

Figure 5.4: Excitation and emission spectra of Sr_2YbF_7:(2Eu-0.75Tm)@Sr_2YF_7 (normalized to their maxima). The indicated transitions correspond to Eu^{3+} ions.

In the excitation and emission spectra (Figure 5.4), intense and sharp emission peaks characteristic of Eu^{3+} ions located in nanocrystalline environments are observed. In the excitation spectrum, the $^5D_0 \rightarrow {}^7F_1$ transition of Eu^{3+} ions is detected at 592 nm, with the $^7F_0 \rightarrow {}^5L_6$ transition at 394 nm standing out. More peaks are observed at 340, 375 and 470 nm, corresponding to the indicated transitions. In the emission spectra, Eu^{3+} ions are excited at 394 nm, corresponding to the $^7F_0 \rightarrow {}^5L_6$ transition, where characteristic emission peaks at 570, 593, 612 and 700 nm are observed, corresponding to the indicated transitions. Figure 5.5 shows the energy levels diagram of Eu^{3+} ion and the named emissions and excitations.
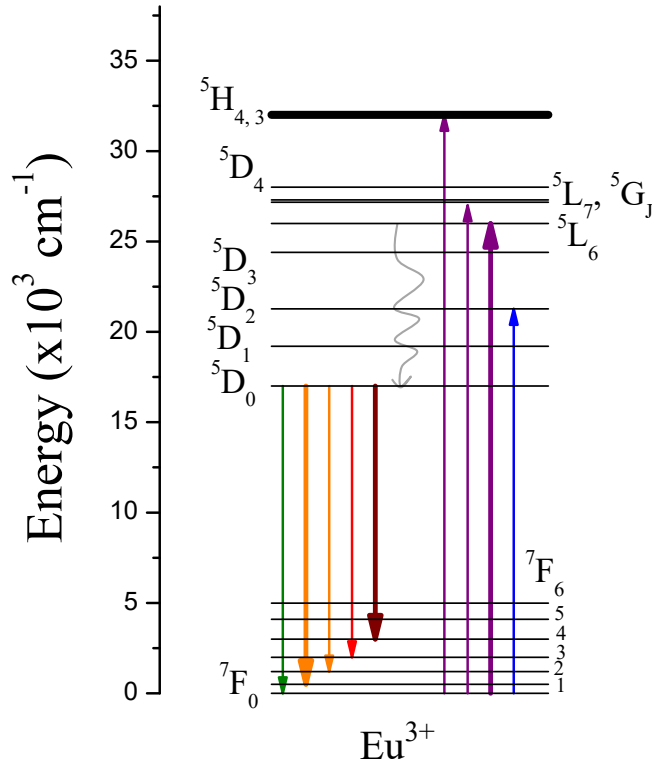

Figure 5.5: Energy levels diagram of Eu^{3+} ion. Straight coloured lines represents the different emissions and excitations of the Eu^{3+} ion (see Figure 5.4). Gray curly arrows indicate non-radiative decay processes.

As it has been said, the Eu^{3+} ions are used as a witness (probe ion) to know the environment in which they are placed. This is because the magnetic dipole $^5D_0 \rightarrow {}^7F_1$ transition is not sensitive to the local environment of the ions, while the $^5D_0 \rightarrow {}^7F_2$ transition is. Therefore, the ratio between these transitions, known as the *asymmetry ratio* (R), accounts for the local environment of these ions, how close it is to being centrosymmetric. For the Core and C@S NPs, the asymmetry ratio is around R = 0.25. This value indicates that the Eu^{3+} ions are located in a very centrosymmetric geometry luminescent center. [23]

As can be inferred from Figure 5.4, the addition of an inert shell (C@S) results in a signal enhancement of 3.3 times with respect the Core. In the Core@Shell the emitting ions (in this case Eu^{3+}) that are close to the surface are protected, reducing the quenching effect. *Quenching* refers to any process that reduces the emission intensity of a sample [24]. In fact, one of the strategies used to reduce this phenomenon is the growth of inert shells, but there are also others such as increasing the excitation power [25].

In this case, the *quenching* phenomenon is due to the presence of oleic acid (used as surfactant in the synthesis of the materials) on the surface of the NPs. These organic species reduce the emission of the Eu^{3+} ions closest to the surface, therefore, the addition of an inert shell leads to the removal of the oleic acid molecules from the boundaring ions of the Core. With this separation, there will be more emitting ions, increasing the intensity of the signal. To check and support this argument, infrared spectroscopy measurement of Sr_2YbF_7:(2Eu-0.75Tm) was carried out, see Figure 5.6. The IR spectrum shows peaks at 2923 cm^{-1} and 2850 cm^{-1} corresponded to the symmetric stretching vibrations of CH_2 bonds. The peak at 1705 cm^{-1} is related with the stretching vibration of C=O bond. It also shows peaks at 1545 cm^{-1} and 1445 cm^{-1} related with the asymmetric and symmetric stretching vibration of $-COO^{-}$ group, respectively. Absorption peak at 3395 cm^{-1}, related with symmetric stretching vibration of -OH, indicate the presence of H_2O molecules. Absorption peak at 968 cm^{-1} also appear.

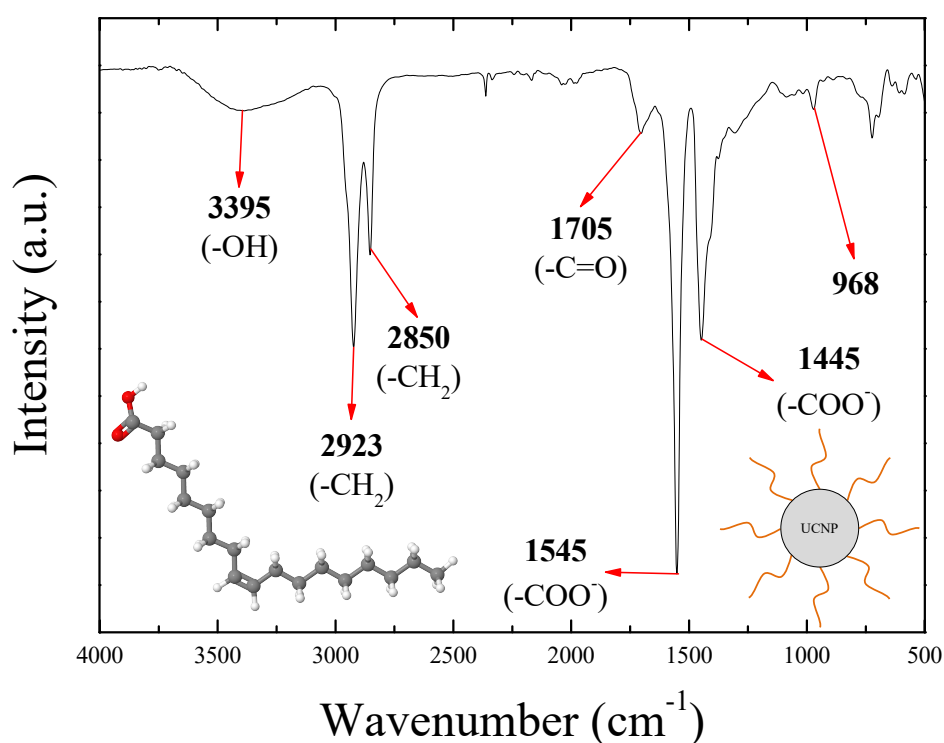Figure 5.6: IR spectrum of Sr_2YbF_7:(2Eu-0.75Tm) to verify the presence of oleic acid (bottom left molecule) on the surface. The bottom right image represents a NP and oleic acid molecules on its surface (orange curved lines).

The above underline the importance of the inert shells applies to all other synthesised materials. Thus, to improve the overall emission of a NP, inert shell should be added. In order to study applications in photocatalysis and photodynamic therapy, this global emission enhancement strategy will be used for samples with strong UV and VIS emissions, respectively.

5.2.2. Tm^{3+} and Gd^{3+}-Tm^{3+} doped NPs

The following spectroscopic study will focus on the analysis of the up-conversion emissions of 0.75Tm^{3+} and 50Gd^{3+}-0.75Tm^{3+} doped NPs, as well as the energy transfer mechanisms that take place.

The up-conversion emission spectra shown in Figures 5.7 and 5.10 are obtained by the excitation of the 0.75Tm^{3+} and 50Gd^{3+}-0.75Tm^{3+} doped NPs with a 300 mW infrared (980 nm) laser, respectively.

Figure 5.7 shows intense and efficient up-conversion emission achivement (which can be seen with the naked eye as shown in the photo of the sample), composed of several emission bands assigned to electronic transitions of Tm^{3+} ions, according to the energy level diagram of Figure 5.8. Strong UV emissions from $^1I_6$ energy level are observed at 290 and 350 nm, which are even more intense than the VIS ones (blue range at 450-470 nm and red range at 650 nm). In addition, weaker infrared emissions at 800 nm are also observed. All transitions related to these emissions are indicated in the graph.
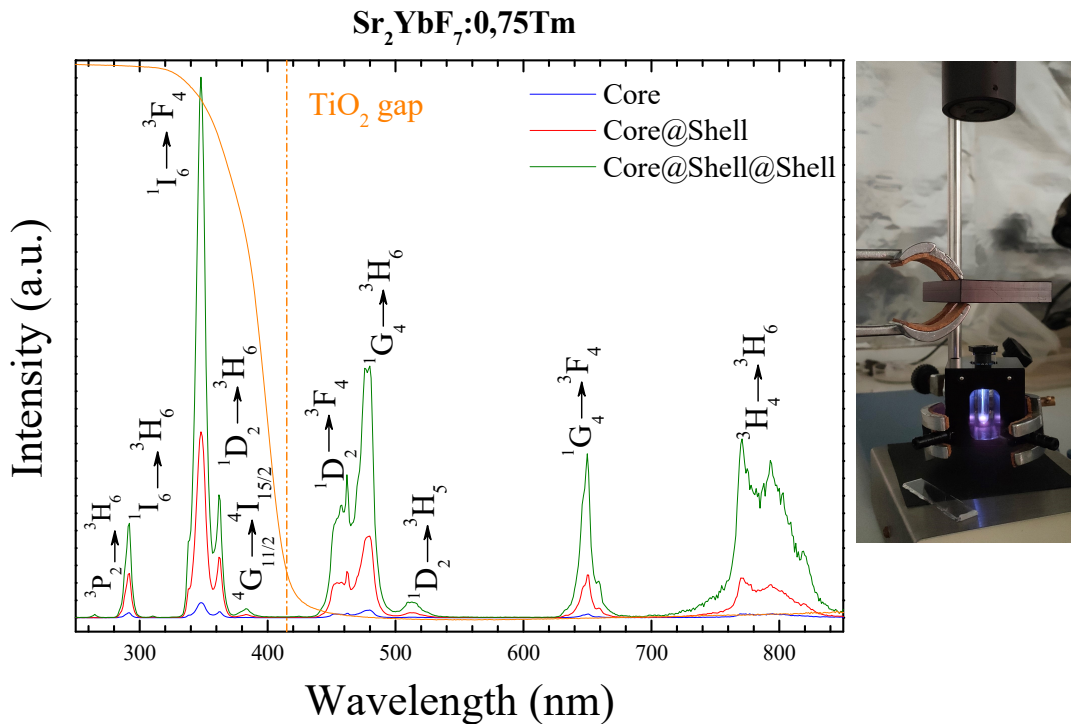

Figure 5.7: Up-conversion emission spectra of the indicated NP (0.75%Tm^{3+}).

The up-conversion phenomenon of Yb^{3+} and Tm^{3+} ions is described as follows (see Figure 5.8). As it has been said earlier, the $^2F_{7/2} \rightarrow {}^2F_{5/2}$ transition of Yb^{3+} ions with a large absorption cross-section is perfectly resonant with the pump radiation of 980 nm. Then the Yb^{3+} ions present in NPs absorbs the incident infrared radiation and they are promoted to the corresponding excited state. Subsequently, efficient energy transfer (ET) processes from Yb^{3+}: $^2F_{5/2}$ to Tm^{3+} ions, directly or by energy migration processes between Yb^{3+} in the crystalline sublattice (see Figure 5.9), populate $^3H_5$, $^3F_{2,3}$ and $^1G_4$ levels. The $^1D_2$ level of Tm^{3+} ions cannot be populate directly by ET from Yb^{3+} ions, so the cross-relaxation ET process involving $^3F_{2,3}$, $^3H_4$ and $^3H_6$ allows to populate the $^1D_2$ level. Finally, the $^1I_6$ level is populated by ET from the Yb^{3+} ions.
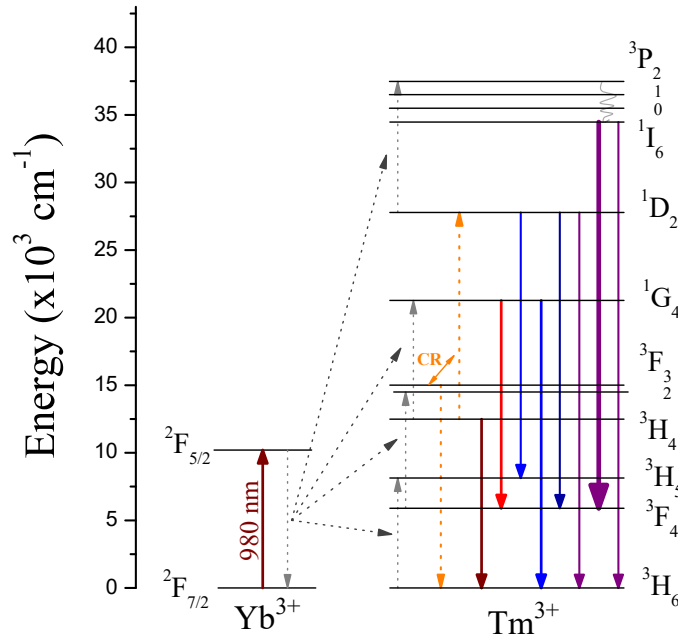
Figure 5.8: Up-conversion phenomenon in Tm^{3+} doped NPs. Straight coloured lines represents the different emissions of the samples (see Figure 5.7), gray dotted lines represents the excitation of the emitter ions and straight black dotted lines represents the energy transfer from Yb^{3+} ions to Tm^{3+}. The orange dotted lines represent the cross-relaxation process (CR) and gray curly arrows indicate non-radiative decay processes.

In order to increase the UV emission of the samples with Tm^{3+}, they are coated with up to two Sr_2YF_7 inert shells. It is observed that the thickness of these shells are 1.66 nm for the first shell and 1.16 nm for the second one, according to XRD measurements. Thus, the addition of a first inert shell results in an increment of the signal of 12 times respect the core NPs. If two inert shells are grown, a signal increase of up to 8 times compared to the C@S sample is achieved; thus, the signal is 36 times more intense than that of the core.

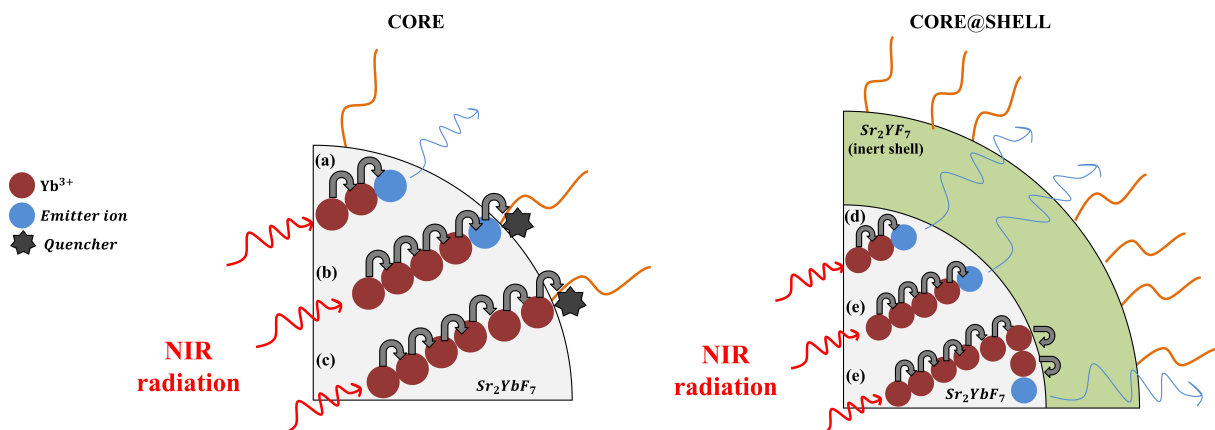Figure 5.9: Schematic illustration of the energy migration and quenching phenomenon in NPs. It is depicted (a) ET towards emitter ions and radiative emission of these; (b) loss of emission due to quenching effect; (c) loss of energy migration due to quenching effect; (d), (e) and (f) effect of the addition of an inert shell on the previous phenomena [26]. All this is applicable to the rest of NPs.

Alternatively, the use of $50Gd^{3+}$-$0.75Tm^{3+}$ NPs is also studied, in order to obtain strong UV emissions of Gd^{3+} ions.

The Sr_2YbF_7:(50Gd-0.75Tm) up-conversion spectra shows the same Tm^{3+} emissions as $0.75Tm^{3+}$ doped NPs, along with characteristic Gd^{3+} ion peaks with the one at 311 nm standing out. In addition, UV emissions associated to Gd^{3+} can be observed from 250 to 310 nm, see left inset in Figure 5.10.
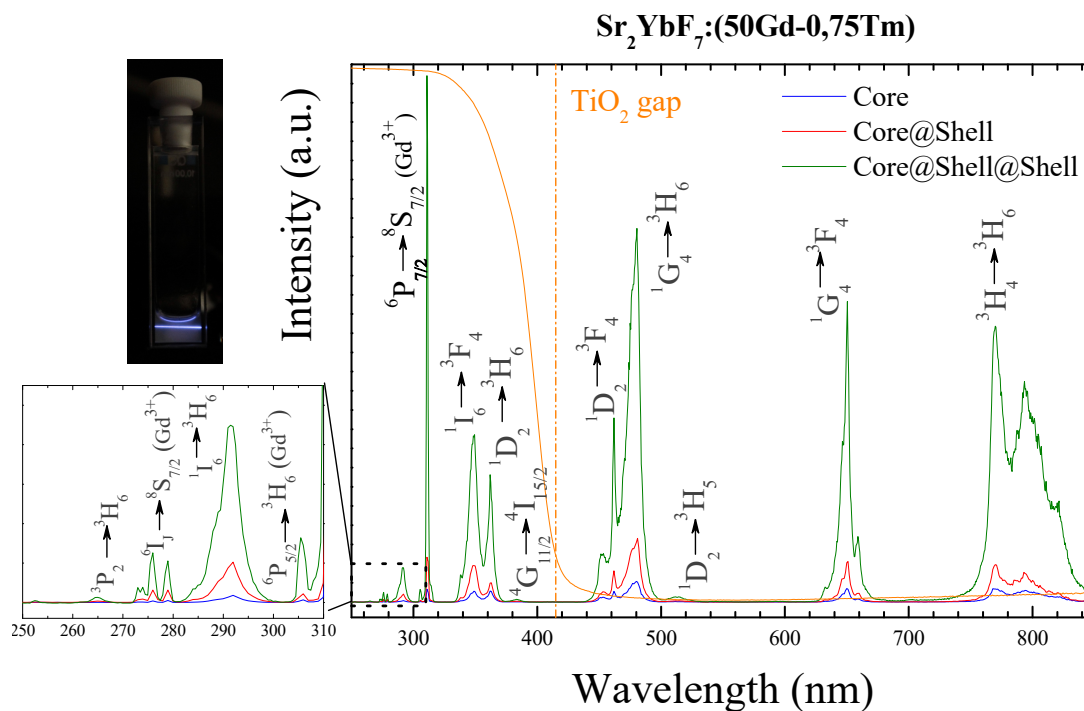

Figure 5.10: Up-conversion emission spectra of the indicated NPs (50%Gd^{3+}-0.75%Tm^{3+}).

For the Sr_2YbF_7:(50Gd-0.75Tm) NPs the up-conversion phenomenon that occurs is similar to the previously described for the Sr_2YbF_7:0.75Tm NPs, except that in this case, the Tm^{3+} ions excited at $^3P_2$ level can additionally transfer energy to Gd^{3+}, taking it to levels ^6I_J, from which UV emission at 276 nm occurs or non-radiative de-excitation to $^6P_{7/2}$ level occurs (see Figure 5.11). The de-excitation from this level leads to intense UV emission at 311 nm, as discussed above. This intense Gd^{3+} UV emission, reveals a very efficient energy transfer mechanism from Tm^{3+} ions to these ions.
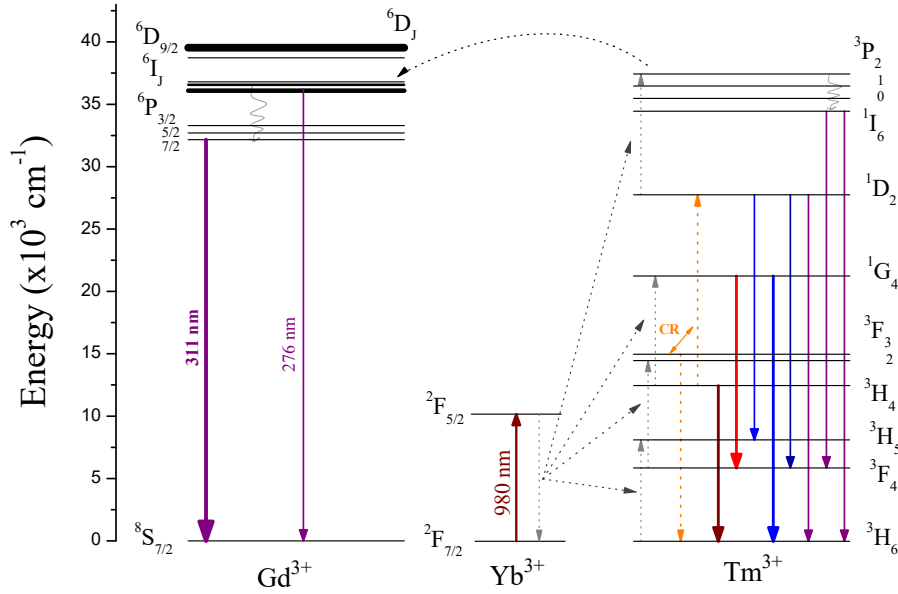
Figure 5.11: Up-conversion phenomenon in Tm^{3+}, Gd^{3+} doped NPs. Straight coloured lines represents the different emissions of the samples (see Figure 5.10), gray dotted lines represent the excitation of the emitter ions and straight black dotted lines represent the energy transfer from Yb^{3+} ions to Tm^{3+}. The orange dotted lines represent the cross-relaxation process (CR) and the curved black dotted line represent the energy transfer from Tm^{3+} ions to Gd^{3+}. Gray curly arrows indicate non-radiative decay processes.

It is observed that the thickness of Gd-Tm doped NPs' shells are 0.865 nm for the first one and 1.065 nm for the second one, according to XRD measurements. In this case, the addition of one inert shell results in a signal 8 times higher than for the core NPs. If two inert shells are grown, a signal increase of up to 11 times compared to the C@S sample is achieved; therefore, the signal is 33 times more intense than that of the core.

For photocatalysis applications, intense UV emissions are of great interest. In the up-conversion emission spectra (Figures 5.7 and 5.10) the dotted orange curve represent the absorption spectrum of TiO_2, which is used as photocatalyst. As can be seen, the activation limit of TiO_2 is indicated to be around 415 nm; any shorter wavelength emission will cause the activation of this complex (see absorption spectrum of TiO_2). Thus, the strong UV emissions of both, $0.75Tm^{3+}$ and $50Gd^{3+}$-$0.75Tm^{3+}$ doped NPs, can be used to activate the TiO_2 complex.

Therefore, the up-conversion phenomenon take place in the studied NPs. It is observed that up to 5 energy transfers, i.e. 5 infrared incident photons, are needed to bring the Tm^{3+} ions to the highest energy level. Nevertheless, due to the high concentration of Yb^{3+} ions in these NPs, a curious phenomenon occurs in which the number of photons needed to excite the Tm^{3+} and Gd^{3+} ions is lower than expected. This is due to a competition mechanism between the linear decay of the emitting ions and the UC process explained above. Therefore, if the excitation processes are dominant, the number of photons observed to reach higher energy levels will be lower.

To check this, a study of the emission intensity (I) versus the pumping power (P) of the diode laser is carried out. In particular, the $I = P^n$ dependence is analysed, where n is the number of absorbed infrared photons. Figures 5.12a and 5.12b show the emission spectra of $Sr_2YbF_7{:}0.75Tm@Sr_2YF_7@Sr_2YF_7$ and $Sr_2YbF_7{:}(50Gd{-}0.75Tm)@Sr_2YF_7@Sr_2YF_7$ for different pumping powers. It can be observed that the emission intensity decreases as the pumping power decreases.

(a) C@S@S Tm^{3+} doped NPs

(b) C@S@S Gd^{3+}-Tm^{3+} doped NPs
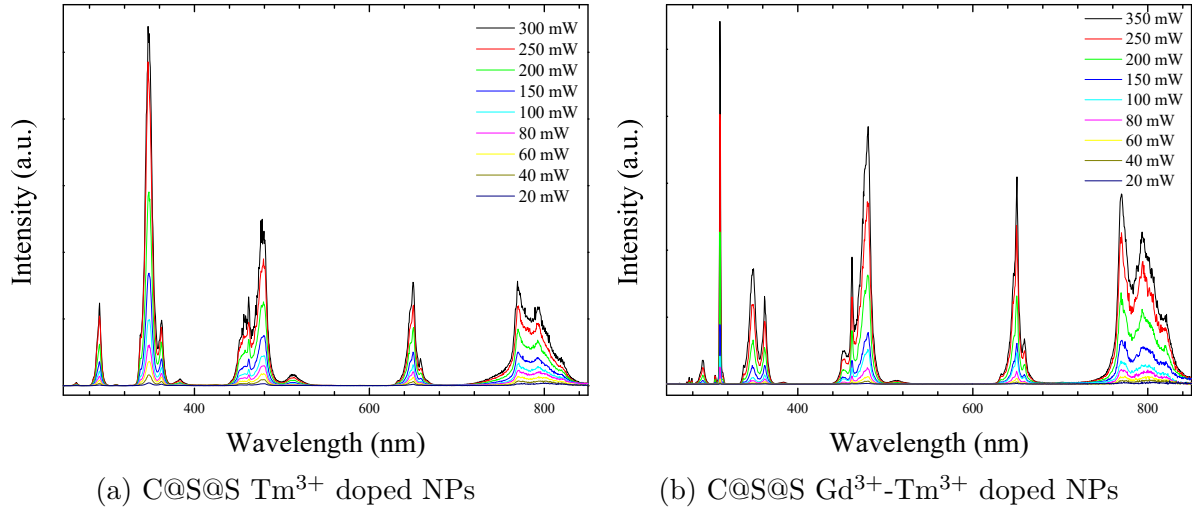
Figure 5.12: NPs' up-conversion spectra for different pump powers.

Figure 5.13 shows a logarithmic representation of intensity versus incident power for the different samples, so that the slope of these curves corresponds to the number of photons n needed to reach the emitting energy level in each case. This value has been obtained by a linear fit of the data for each emission and the results are shown in Table 5.2.

(a) Tm^{3+} doped NPs

(b) Gd^{3+}-Tm^{3+} doped NPs
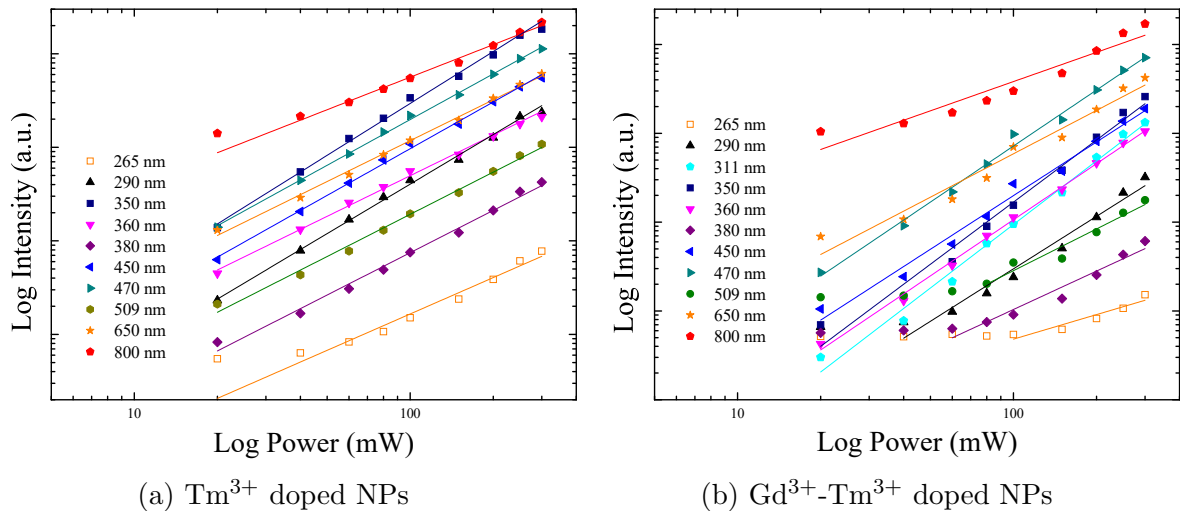
Figure 5.13: Logarithmic representation of intensity versus incident power for the different samples.

Transition (λ)	Number of photons (n) Expected	Observed 0.75%Tm^{3+}	Observed 50%Gd^{3+}-0.75%Tm^{3+}
$^3P_2 \rightarrow {}^3F_4$ (265 nm)	5	1.29	-
$^1I_6 \rightarrow {}^3H_6$ (290 nm)	5	1.76	1.96
$^6P_{7/2} \rightarrow {}^8S_{7/2}$ (311 nm)	5	-	2.38
$^1I_6 \rightarrow {}^3F_4$ (350 nm)	5	1.84	2.32
$^1D_2 \rightarrow {}^3H_6$ (360 nm)	4	1.44	2.10
$^1D_2 \rightarrow {}^3H_6$ (380 nm)	3	1.50	1.44
$^1D_2 \rightarrow {}^3F_4$ (450 nm)	4	1.66	2.01
$^1G_4 \rightarrow {}^3H_6$ (470 nm)	3	1.62	2.10
$^1D_2 \rightarrow {}^3H_5$ (509 nm)	4	1.50	1.56
$^1G_4 \rightarrow {}^3F_4$ (650 nm)	3	1.45	1.62
$^3H_4 \rightarrow {}^3H_6$ (800 nm)	2	1.16	1.09

Table 5.2: Expected and observed number of photons in up-conversion processes for the indicated transitions (emissions) seen in Figures 5.7 and 5.10.

The number of photons n observed are significantly lower than the expected ones for all the studied transitions. The reason is the high concentration of Yb^{3+} ions compared to that of Tm^{3+} ions, since in the high excitation power regime the up-conversion processes described above are dominant over the de-excitation processes. It is obvious from Figure 5.13 that for a regime of low incident radiation power, the slope of the curve is different from that of the high power regime (however, in these cases the slope is practically zero, concluding that no up-conversion processes take place and the Tm^{3+} ions are not led to high energy levels as this is particularly true for the more energetic emissions, UV, and not for the less energetic ones, 650 and 800 nm).

Note also that for Sr$_2$YbF$_7$:(50Gd-0.75Tm)@Sr$_2$YF$_7$@Sr$_2$YF$_7$ NPs, the number of observed photons needed is higher than for Sr$_2$YbF$_7$:0.75Tm@Sr$_2$YF$_7$@Sr$_2$YF$_7$ samples, especially for UV emissions (which, theoretically, require more photons to be achieved). This is due to the high concentration of Gd^{3+} ions (50%), replacing the Yb^{3+} ions in the matrix (as discussed in the structural characterisation) which decreases the amount of sensitisers for the up-conversion process. Thus the high concentration of Yb^{3+} ions as sensitiser favourable to and achieves a high efficiency of up-conversion processes.

From these results, it is concluded that efficient up-conversion processes take place in the material studied in this section, achieving intense UV emissions able to activate TiO$_2$ for photocatalytic applications.

5.2.3. Er^{3+} doped NPs

In order to study the application of NPs in photodynamic therapy, the spectroscopic study of Sr$_2$YbF$_7$:1Er NPs, which shows strong emissions in the visible red range at 660 nm clearly seen with the naked eye, is presented. Figure 5.14 shows the up-conversion emission spectra for the three 1Er^{3+} doped samples. Intense emission is observed in the visible, dominated by the red one (660 nm). Other peaks occur at 380, 410, 540 and 820 nm. The transitions associated with each peak are also indicated. The orange dotted curve represent the absorption spectrum of Methylene Blue (MB), which is used as photosensitizer in the photodynamic therapy. The absorption maximun of MB is at around 664 nm, coinciding with the extremely intense red emission of the Sr$_2$YbF$_7$:1Er NPs.
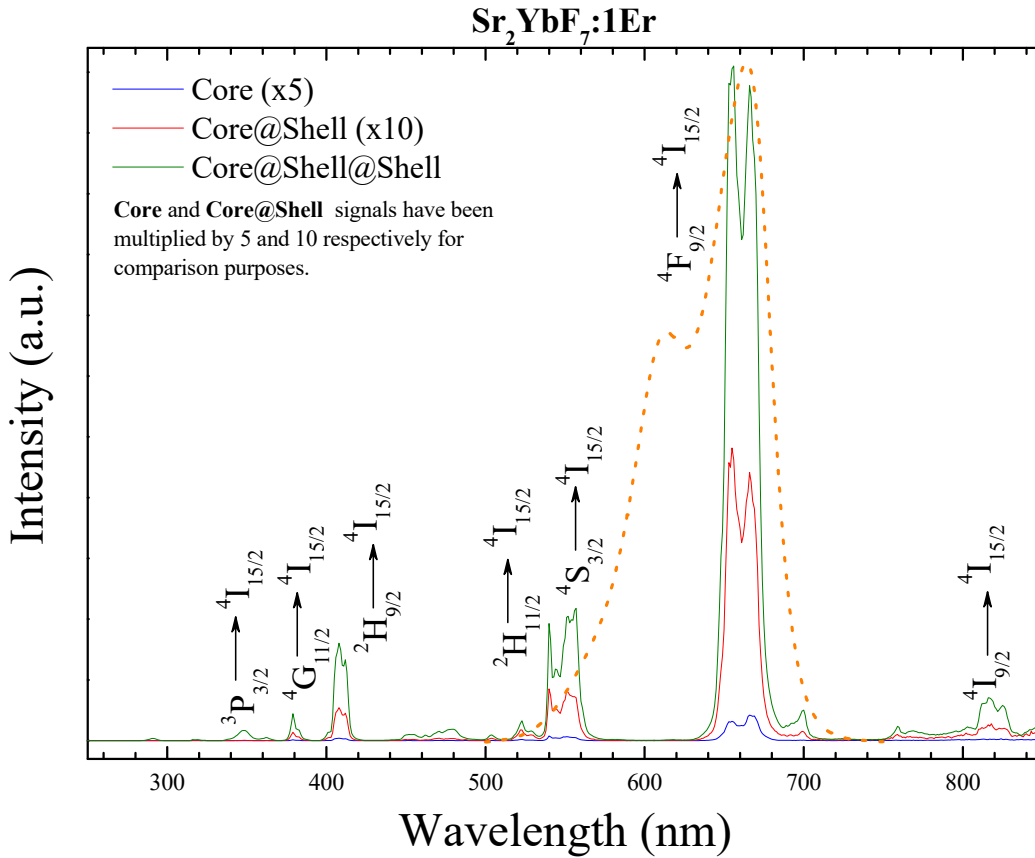

Figure 5.14: Up-conversion emission spectra of 1Er^{3+} doped NPs. The Core and Core@Shell spectra have been multiplied by 5 and 10 respectively for comparison purposes.

The up-conversion phenomenon of Yb^{3+} and Er^{3+} ions is described as follows (see Figure 5.15). The ^{2}F$_{7/2} \rightarrow$ ^{2}F$_{5/2}$ transition of the Yb^{3+} ions presents a larger absorption cross-section than the ^{4}I$_{15/2} \rightarrow$ ^{4}I$_{11/2}$ transition of the Er^{3+} ions. Then the Yb^{3+} ions present in the NPs absorbs the majority the incident infrared radiation and they are promoted to the corresponding excited state. Subsequently, efficient energy transfer processes from Yb^{3+}: ^{2}F$_{5/2}$ to Er^{3+} ions, directly or by energy migration processes between Yb^{3+} in the crystalline sublattice, populate ^{4}F$_{7/2}$ and ^{2}H$_{11/2}$ (or ^{4}S$_{3/2}$) by 2-photon processes, ^{4}G$_{11/2}$ and ^{2}H$_{9/2}$ levels by 3-photon processes and ^{2}P$_{3/2}$ level by 4-photon processes. The high Yb^{3+} concentration leads to cross-relaxation processes in Er^{3+} ions and back energy transfer to Yb^{3+} ions, which favours the red emission against the green one [27].
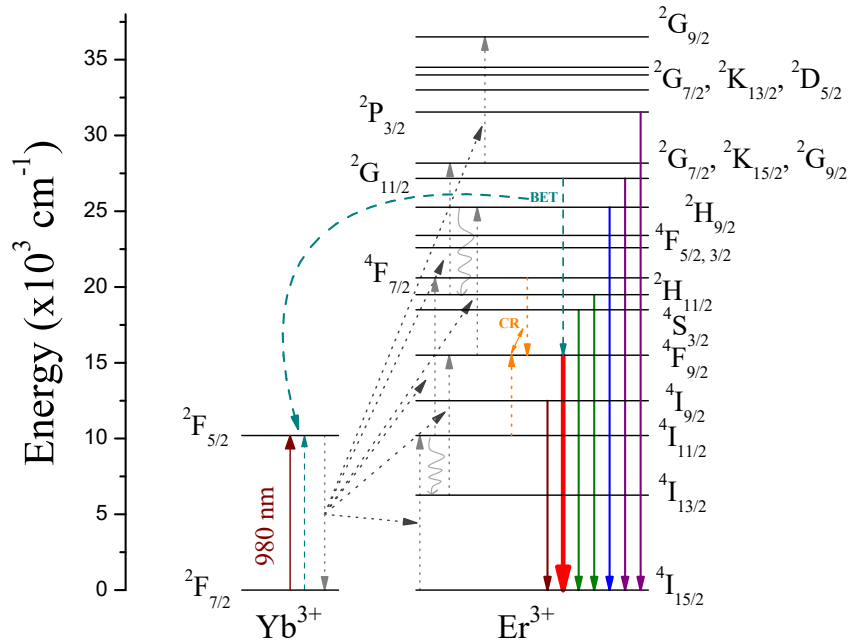
Figure 5.15: Up-conversion phenomenon in Er^{3+} doped NPs. Straight coloured lines represents the different emissions of the sample (see Figure 5.14), gray dotted lines represents the excitation of the emitter ions, black dotted lines represents the energy transfer from Yb^{3+} ions to Er^{3+}, orange dotted lines represent cross-relaxation processes (CR) and turquoise dashed lines represent the back energy transfer process (BET). Gray curly arrows indicate non-radiative decay processes.

According to XRD measurements, for the $1Er^{3+}$ doped NPs the shell thicknesses are 1.425 nm for the first one and 1.305 nm for the second one. The addition of an inert shell results in a signal 6.24 times higher than for the "bare" (core) NPs. If two inert shells are grown, a signal increase of up to 50 times compared to the core@shell sample is achieved; therefore, the signal is 143 times more intense than that of the core.

In order to study medical applications in photodynamic therapy, the global emission enhancement due to the addition of inert shells and the intense red emissions of these NPs are of great interest.

Universidad
de La Laguna

5.3. Photocatalytic applications: MB degradation experiment

In view of the intense UV emission and the efficient up-conversion processes that take place in Sr_2YbF_7:0.75Tm@Sr_2YF_7@Sr_2YF_7 and Sr_2YbF_7:(50Gd-0.75Tm)@Sr_2YF_7@Sr_2YF_7 NPs, a study of their potential use in photocatalytic processes was carried out.

For the study of wastewater treatment, Methylene Blue (MB) is widely used as a model pollutant and the TiO_2 is one of the most common semiconductor photocatalysts. The heterogeneous TiO_2 photocatalytic process required the use of UV radiation, which come from the studied NPs, to operate. Firstly, photons with a higher energy than the semiconductor band gap (in this case $E_{TiO_2} = 3.0$ eV, i.e. 415 nm shorter radiation is needed) generate high energy electron-hole pairs (see Figure 5.16). The electrons in the conductive band and the holes in the valence band are strong reducing and oxidizing agents, respectively. Then electron-hole pairs cause the MB molecules degradation by directly oxidising them or by generating hydroxyl ($^{\cdot}OH$) and superoxide ($^{\cdot}O_2^-$) radicals from water molecules oxidation and molecular oxygen reduction respectively, which also degrade MB molecules.[28] Figure 5.16 shows an schematic diagram of this process.
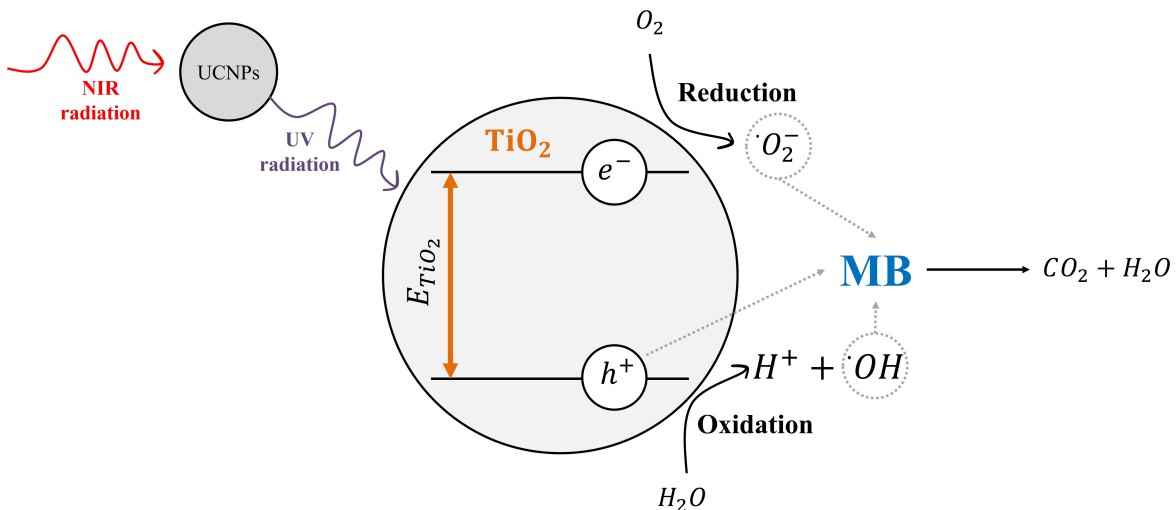

Figure 5.16: Schematic diagram of electron-hole pair formation in TiO_2 under UV radiation (from UCNPs) and the resulting MB degradation. The black curved lines represent the radicals formation and the gray dotted lines indicates the indicates those involved in the degradation of MB. The resulting products are also indicated.

On the other hand, the adsorption effect when mixing TiO_2 and MB must be taken into account, as the MB molecules cling to the semiconductor surface and are separated from the aqueous phase.

Figure 5.17 shows the reference MB absorption spectra (with the maximun absorption at around 664 nm, DO = 2.0), the adsorption effect in the solution absorption spectra and the absorption curve corresponding to the MB photodegradation for each NP. It presents evidence of photocatalytic degradation of the MB as it can be observed a change in the absorbance spectra of the MB aqueous solution. For Sr_2YbF_7:0.75Tm@Sr_2YF_7@Sr_2YF_7 NPs a 24% reduction of the MB concentration is obtained related to the TiO_2 adsorption effect, while for Sr_2YbF_7:(50Gd-0.75Tm)@Sr_2YF_7@Sr_2YF_7 NPs a 18% is measured. After 1 hour and 30 minutes of light irradiation, a MB degradation of 38% and 19% was achieved for $0.75Tm^{3+}$ and $50Gd^{3+}$-$0.75Tm^{3+}$ doped NPs, respectively.
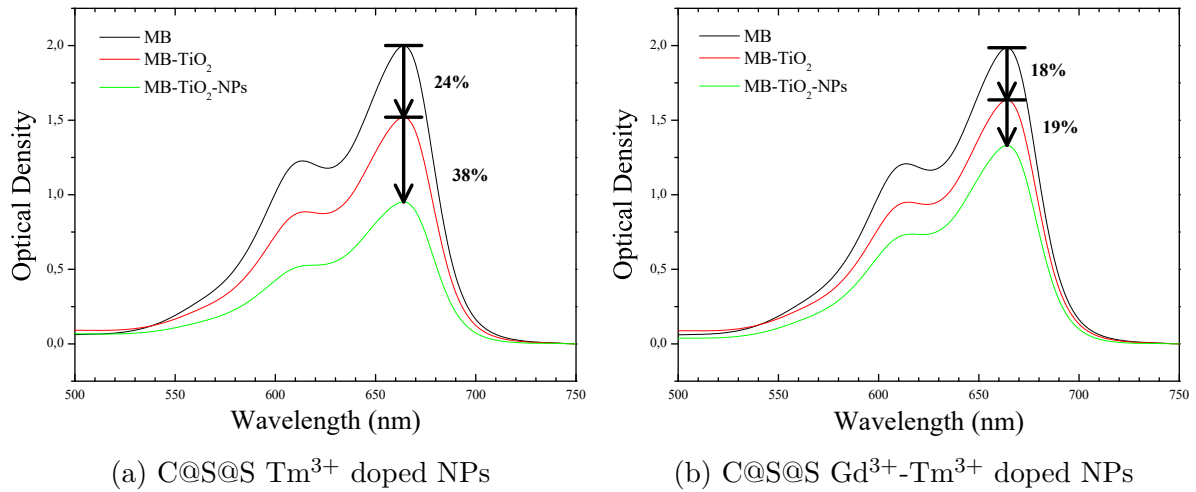
(a) C@S@S Tm^{3+} doped NPs

(b) C@S@S Gd^{3+}-Tm^{3+} doped NPs

Figure 5.17: NPs' emission spectra for different pump powers

For Sr_2YbF_7:0.75Tm@Sr_2YF_7@Sr_2YF_7 NPs, a MB degradation two times higher was obtain that the one for Sr_2YbF_7:(50Gd-0.75Tm)@Sr_2YF_7@Sr_2YF_7 NPs, despite the fact that the 0.75Tm^{3+} doped NPs have a UV emission 4 times more intense than the the 50Gd^{3+}-0.75Tm^{3+} NPs (comparison made for the UV intensity of Figures 5.7 and 5.10). This opens the door to the idea that photodegradation with Gd^{3+} samples is more efficient.

In order to increase the energy transfer efficiency from NPs to TiO_2, different strategies could be explore, such as the possibility of coating the NPs with the chosen semiconductor to obtain a non-radiative ET. Additionally, a more extensive study of the influence of the long lifetime of Gd^{3+} ions, related with its large energy gap, in this ET mechanism can be carried out.

5.4. Medical applications: a first approach to photodynamic therapy

In recent years, the photodynamic therapy is gaining acceptance as a non-invasive and non-expensive medical technique for cancer treatment and, currently, NPs are under study for their use as photosensitizer carriers for deep tissue photodynamic therapy. For photodynamic therapy, photosensitizers are usually activated with visible light, but this does not have a high penetrating power in living tissues. For this reason, up-conversion nanoparticles (UCNPs) are widely studied because they are able of transforming infrared radiation (IR), which strikes tissues with great depth (see Figure 5.18a) and little damage, into visible radiation (VIS), which is used by the chosen photosensitizers.

Figure 5.18b shows the performance of this medical treatment. Normally, synthesised UCNPs have oleic acid molecules on their surface, which makes them hydrophobic; so for medical use, first α-CD molecules must be added to these UCNPs (allowing them to be dispersed in an aqueous solution). Then the α-CD-NPs are loaded with a photosensitizer, in this case Methylene Blue (MB). The treated tissue is irradiated with near infrared (NIR) light, so that the UCNPs are excited and activate the photosensitizers via fluorescence resonance energy transfer (FRET). The activated photosensitizers generate reactive oxygen species, such as $^1O_2$, which is highly toxic for living cells. The resulting cytotoxic species eliminate the cancer cells. From this, it can be concluded the advantages of this therapy, as it is highly localized and does not present lot side effects. [29]
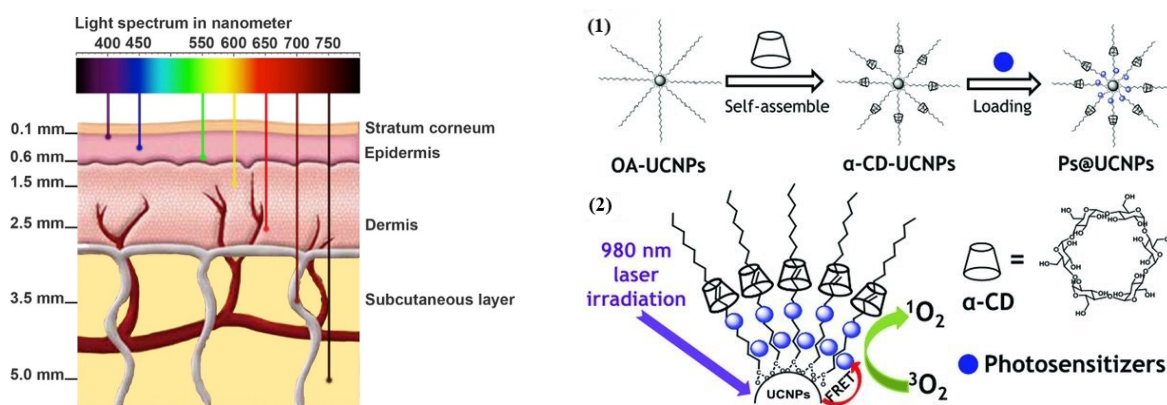
(a) Schematic illustration of different radiation penetration in skin. The IR light can reach deeper layers, which is why it is used.

(b) Schematic illustration of (1) incorporation of photosensitizers into UCNPs and (2) performance of photodynamic therapy. [29, Fig. 1]

Figure 5.18: Photodynamic therapy supporting illustrations.

In light of the intense red emissions of Sr_2YbF_7:1Er NPs, MB is chosen as photosensitizer as it has an absorption maximum around 664 nm. Thus, a first approach to this type of therapy is presented through the spectroscopic study of MB-α-CD-Sr_2YbF_7:1Er NPs.

Figure 5.19 shows the absorbance spectrum of MB and the up-conversion emission spectrum of the MB-α-CD-Sr$_2$YbF$_7$:1Er NPs, at 980 nm. There is a clear decrease in the red emission of the MB-α-CD-Sr$_2$YbF$_7$:1Er NPs compared to the sample without photosensitizers, coinciding with the MB absorption spectrum, while all other emissions remain the same. This indicates efficient FRET from the Er^{3+} ions to the MB. These results leads to consider these materials in photodynamic therapy.
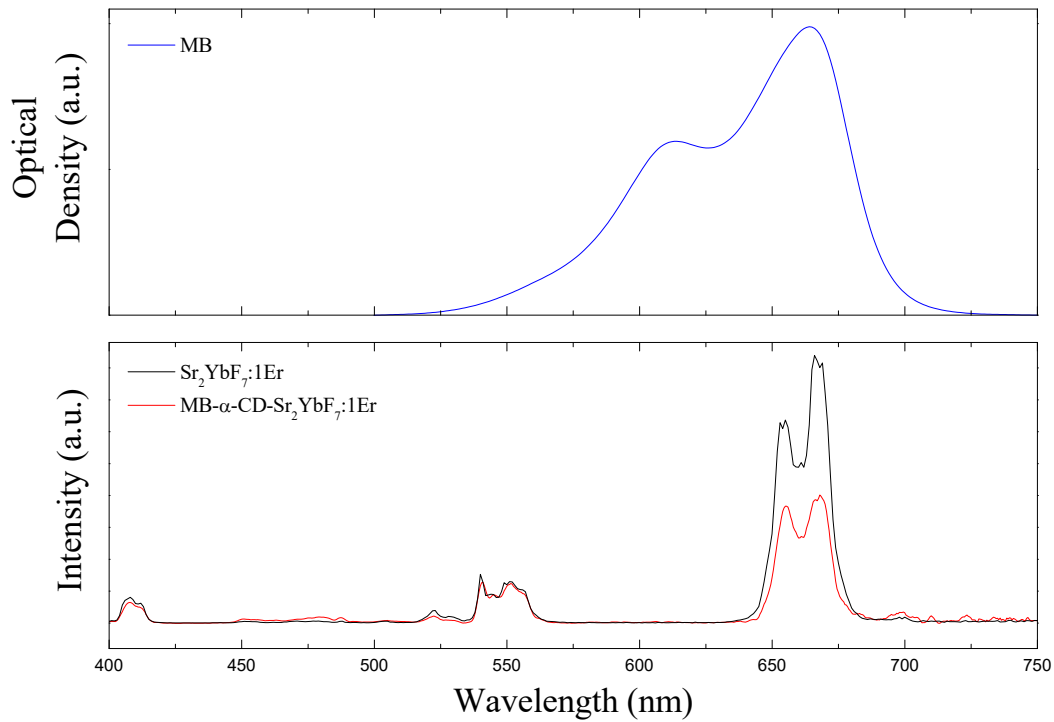

Figure 5.19: Emission spectrum of MB-α-CD-Sr$_2$YbF$_7$:1Er and Sr$_2$YbF$_7$:1Er NPs and MB absorption spectrum.

6.   Conclusions

En este TFG se ha llevado a cabo la síntesis exitosa por el método solvotermal de NPs de Sr_2YbF_7, que han sido dopadas con diferentes iones (RE^{3+}): Eu^{3+} (5%), Tm^{3+} (0.75%), Gd^{3+} (50%) y Er^{3+} (1%). La caracterización estructural mediante medidas de XRD, imágenes TEM-HRTEM y análisis EDS de los materiales sintetizados han revelado la correcta formación de estos con fase tetragonal con tamaños entre 10 y 15 nm. El estudio espectroscópico de las muestras dopadas con $2Eu^{3+}$-$0.75Tm^{3+}$ han revelado la presencia de los iones dopantes en centros de alta centrosimetría; además de la importancia del recubrimiento de las NPs con capas inertes de Sr_2YF_7. Para las NPs dopadas con $0.75Tm^{3+}$ y $50Gd^{3+}$-$0.75Tm^{3+}$, se observaron procesos UC muy eficientes, con intensas emisiones UV para su uso en aplicaciones fotocatalíticas. En las NPs dopadas con $1Er^{3+}$, también se han observado procesos UC muy eficientes con fuertes emisiones en el VIS (dominadas por el rojo) y han repotado un gran aumento de la emisión al ser recubiertas con capas inertes.

En cuanto a las aplicaciones fotocatalíticas, se observó la degradación exitosa del MB cuando el TiO_2 es activado por las muestras dopadas con $0.75Tm^{3+}$ y $50Gd^{3+}$-$0.75Tm^{3+}$. Por otro lado, se ha estudiado el potencial uso de las NPs dopadas con $1Er^{3+}$ en terapia fotodinámica.

The synthesis and an extensive structural and spectroscopic study of different nanomaterials has been carried out: Sr_2YbF_7:(2Eu-0.75Tm), Sr_2YbF_7:0.75Tm, Sr_2YbF_7:(50Gd-0.75Tm) and Sr_2YbF_7:1Er, as well as their potencial photocatalytic and medical applications. The main results are the following:

- **Synthesis of NPs**: different NPs have been satisfactorily obtained by the solvothermal method.

- **Structural Characterisation**: structural analysis based on XRD patterns, TEM-HRTEM images and EDS patterns was performed. The following results stand out:

  - XRD patterns confirmed the obtention of the NPs, revealing a tetragonal phase, without any additional phase. In addition, sizes around 10 nm were achieved. The growth of Sr_2YF_7 inert shells was confirmed with thickness up to 2.82 nm.

  - TEM-HRTEM images confirmed also the formation and uniform distribution of the NPs, as well as the sizes calculated from the XRD patterns.

  - EDS analysis confirmed the presence of Sr, Yb and F as main constituents of NPs with the expected stochiometric ratios, i.e. (2:1:7) ascribed to Sr_2YbF.

Universidad
de La Laguna

- **Spectroscopic study**: the different spectra obtained rounded off the structural characterisation and were used to get a deeper understanding of the energy transfer mechanisms that take place in the NPs. In addition, the effect of growing Sr_2YF_7 inert shells was studied.

  - In order to complete the structural analysis, the $2Eu^{3+}$-$0.75Tm^{3+}$ doped NPs were analysed, where Eu^{3+} ions are used as probe ion, revealing the highly centrosimmetric geometry luminiscent centers present in the materials studied. The presence of oleic acid molecules on the surface of the NPs is also confirmed via IR spectroscopy, which causes the reduction of the emission (*quenching* phenomenon), highlighting the importance of the addition of inert shells.

  - The spectroscopic analysis of $0.75Tm^{3+}$ and $50Gd^{3+}$-$0.75Tm^{3+}$ doped NPs, has revealed that efficient up-conversion phenomena take place, as well as great overall emission enhancement in the coated NPs. In addition, a study of the emission intensity versus the pump power, has revealed the existence of a competition mechanism between the linear decay of the emitting ions and the UC processes. Finally, the intense UV emissions of these materials leads to their potential use in photocatalytic applications.

  - It has also been found that in $1Er^{3+}$ doped NPs efficient up-conversion phenomena take place, with intense VIS emissions, dominated by the red one (660 nm). Additionally, these NPs have reported the biggest emission enhancement when Sr_2YF_7 inert shells are epitaxially grown. Finally, the intense red emissions of these materials leads to their potential use in photodynamic therapy.

- **Photocatalytic applications**: the use of Sr_2YbF_7:$0.75Tm@Sr_2YF_7@Sr_2YF_7$ and Sr_2YbF_7:$(50Gd$-$0.75Tm)@Sr_2YF_7@Sr_2YF_7$ NPs in photocatalytic processes has been studied, in particular, the MB degradation via TiO_2 activation. Around a 20% reduction of MB concentration have been reported, related to the TiO_2 adsorption effect. A MB degradation of 38% and 19% was achieved for $0.75Tm^{3+}$ and $50Gd^{3+}$-$0.75Tm^{3+}$ doped NPs, respectively. In light of these results, it is proposed to coat these NPs with TiO_2 photocatalyst, in order to hone the energy transfer to TiO_2.

- **Medical applications**: the potential use of Sr_2YbF_7:$1Er$ NPs in photodynamic therapy has been studied. The spectroscopic study of the NPs loaded with MB as photosensitizer under NIR radiation, has revealed a clear energy transfer from Sr_2YbF_7:$1Er$ to MB, promising a potential medical use of this NPs.

7. References

[1] Velázquez, A. M. (2011). *Una revolución en miniatura: Nanotecnología al servicio de la humanidad.* Universitat de València.

[2] British Museum: drinking-cup. (2021). *The Lycurgus cup* The British Museum. `https://www.britishmuseum.org/collection/object/H_1958-1202-1`

[3] Willard, M. A., Kurihara, L. K., Carpenter, E. E., Calvin, S., and Harris, V. G. (2004). *Chemically prepared magnetic nanoparticles.* International materials reviews, 49(3-4), 125-170.

[4] Khan, I., Saeed, K., and Khan, I. (2019). *Nanoparticles: Properties, applications and toxicities.* Arabian journal of chemistry, 12(7), 908-931.

[5] Zhu, X., Su, Q., Feng, W., and Li, F. (2017). *Anti-Stokes shift luminescent materials for bio-applications.* Chemical Society Reviews, 46(4), 1025-1039.

[6] Edinburgh Instruments Ltd. (2021, 25 noviembre). *Blog: What is upconversion?.* Edinburgh Instruments. `https://www.edinst.com/blog/photon-upconversion/`

[7] Dhand, C., Dwivedi, N., Loh, X. J., Ying, A. N. J., Verma, N. K., Beuerman, R. W., ... and Ramakrishna, S. (2015). *Methods and strategies for the synthesis of diverse nanoparticles and their applications: a comprehensive overview.* Rsc Advances, 5(127), 105003-105037.

[8] Li, X., Cao, J., Wei, Y., Yang, Z., and Guo, H. (2015). *Optical thermometry based on up-conversion luminescence behavior of Er3+-doped transparent Sr2YbF7 glass-ceramics.* Journal of the American Ceramic Society, 98(12), 3824-3830.

[9] del-Castillo, J., Mendez-Ramos, J., Acosta-Mora, P., and Yanes, A. C. (2022). *Upconversion photonics in solvothermal Sr2YbF7: Tm3+@ Sr2YF7 core-shell nanocrystals for enhanced photocatalytic degradation of pollutants.* Journal of Luminescence, 241, 118490.

[10] Shannon Radii. (s. f.). *Database of Ionic Radii.* `http://abulafia.mt.ic.ac.uk/shannon/ptable.php`

[11] Jha, A. (2016). *Inorganic Glasses for Photonics: Fundamentals, Engineering, and Applications.Chapter 6: Spectroscopic properties of Lanthanide (Ln^{3+}) and transition metal (M^{3+})-ion doped glasses* (pp.209-260). John Wiley and Sons.

[12] Raymond, K. N., Wellman, D. L., Sgarlata, C., and Hill, A. P. (2010). *Curvature of the lanthanide contraction: An explanation.* Comptes Rendus Chimie, 13(6-7), 849-852.

[13] De Decker, J. (2017). *Functionalized metal-organic frameworks as selective metal adsorbents* (Doctoral dissertation, Ghent University).

[14] del Río, C. S. (2020). *Física cuántica. Parte tercera: Átomos. Capítulo 23: Átomos multielectrónicos.* Ediciones Pirámide.

Universidad
de La Laguna

[15] Van Der Ende, B. M., Aarts, L., and Meijerink, A. (2009). *Lanthanide ions as spectral converters for solar cells*. Physical Chemistry Chemical Physics, 11(47), 11081-11095.

[16] Rettori, C., Davidov, D., and Kim, H. M. (1973). *Crystalline-field effects in the EPR of Er in various cubic metals*. Physical Review B, 8(11), 5335.

[17] Fischer, S., Mehlenbacher, R. D., Lay, A., Siefe, C., Alivisatos, A. P., and Dionne, J. A. (2019). *Small alkaline-earth-based core/shell nanoparticles for efficient upconversion*. Nano letters, 19(6), 3878-3885.

[18] Li, J., Wu, Q., and Wu, J. (2016). *Synthesis of Nanoparticles via Solvothermal and Hydrothermal Methods 12*.

[19] X'Pert3 MRD - XRPD - *Sistema XRD de investigación de materiales*. (2022). Malvern Panalytical. `https://www.malvernpanalytical.com/es/products/product-range/xpert3-range/xpert3-mrd#howitworks`

[20] JEM-2100 Electron Microscope - Products - JEOL Ltd. (2022). *Electron Microscopy Specifications*. `https://www.jeol.co.jp/en/products/detail/JEM-2100.html`

[21] Muniz, F. T. L., Miranda, M. R., Morilla dos Santos, C., and Sasaki, J. M. (2016). *The Scherrer equation and the dynamical theory of X-ray diffraction*. Acta Crystallographica Section A: Foundations and Advances, 72(3), 385-390.

[22] Simon, S. H. (2013). *The Oxford solid state basics*. OUP Oxford.

[23] Kolesnikov, I. E., Povolotskiy, A. V., Mamonova, D. V., Kolesnikov, E. Y., Kurochkin, A. V., Lähderanta, E., and Mikhailov, M. D. (2018). *Asymmetry ratio as a parameter of Eu3+ local environment in phosphors*. Journal of Rare Earths, 36(5), 474-481.

[24] Lakowicz, J. R. (1983). *Quenching of fluorescence. Principles of fluorescence spectroscopy*, 257-301.

[25] Wen, S., Zhou, J., Zheng, K., Bednarkiewicz, A., Liu, X., and Jin, D. (2018). *Advances in highly doped upconversion nanoparticles*. Nature communications, 9(1), 1-12.

[26] Han, S., Qin, X., An, Z., Zhu, Y., Liang, L., Han, Y., ... and Liu, X. (2016). *Multicolour synthesis in lanthanide-doped nanocrystals through cation exchange in water*. Nature communications, 7(1), 1-7.

[27] Schroter, A., Märkl, S., Weitzel, N., and Hirsch, T. (2022). *Upconversion Nanocrystals with High Lanthanide Content: Luminescence Loss by Energy Migration versus Luminescence Enhancement by Increased NIR Absorption*. Advanced Functional Materials, 2113065.

[28] Mora, P. A. (2020). *Rare-earth doped up-conversion materials for photocatalysis and photonic applications* (Doctoral dissertation, Universidad de La Laguna).

[29] Tian, G., Ren, W., Yan, L., Jian, S., Gu, Z., Zhou, L., ... and Zhao, Y. (2013). *Red-Emitting upconverting nanoparticles for photodynamic therapy in cancer cells under near-infrared excitation*. Small, 9(11), 1929-1938.

Universidad
de La Laguna